1-30-2013

Behavior and measurement of distributed sources in a shielding matrix using gamma spectroscopy

Jacob Miller

Follow this and additional works at: https://digitalrepository.unm.edu/ne_etds

Jacob Miller

Candidate

Chemical and Nuclear Engineering

Department

This thesis is approved, and it is acceptable in quality and form for publication:

Approved by the Thesis Committee:

Dr. Cassiano de Oliveira , Chairperson

Dr. Gary Cooper

Dr. Kenya da Cunha

Behavior and Measurement of Distributed Sources in a
Shielding Matrix Using Gamma Spectroscopy

by

Jacob Miller

Bachelors of Science, Engineering Physics and Nuclear Engineering

THESIS

Submitted in Partial Fulfillment of the Requirements for the Degree of

Master of Science

Nuclear Engineering

The University of New Mexico

Albuquerque, New Mexico

December, 2012

ii

Behavior and Measurement of Distributed Sources in a

Shielding Matrix Using Gamma Spectroscopy

by

Jacob Miller

B.S., Engineering Physics and Nuclear Engineering,

Rensselaer Polytechnic Institute, 2002

Abstract

As part of its mission, the Department of Energy generates transuranic waste materials. Some of these wastes are present in large waste containers. The accurate assay of these waste materials in large containers poses unique challenges. These wastes have radioactive sources that are spread throughout the container with a variety of waste matrices that provide shielding.

Although multiple well established and validated methods that use active and/or passive neutron detection in conjunction with gamma spectroscopy exist to assay these waste materials, these methods are expensive and not readily available at any given facility. As a result, less expensive alternatives, such as gamma spectroscopy alone, are often used.

This paper researches the impact of a distributed shielding medium on a distributed transuranic source and the physical limitations of using gamma spectroscopy alone, without the benefit of either active or passive neutron counting. This included comparing the assay results from a gamma spectroscopy based system to one that uses passive neutron counting in addition to gamma spectroscopy. The differences between these

systems were noted, and then evaluated through modeling using MCNPX to determine

the cause of the observed discrepancies.

Table of Contents

List of Tables

List of Figures

Chapter 1 Introduction

1.1   Transuranic Waste

The Department of Energy's (DOE's) weapons and research programs generate a number of different types of radioactive wastes. These radioactive waste streams fall into a number of different categories based on the general characteristics, including the potential for radiological consequences to the public, workers, and the environment.

One of the more significant categories of radioactive waste generated by the DOE from a potential dose consequence perspective is Transuranic (TRU) waste, which is defined in the DOE complex as waste containing isotopes with an atomic number higher than 92 at a concentration of greater than 100 nCi/g as well as having a half-life of longer than 20 years (Ref. 1). TRU wastes are predominately alpha emitters, and therefore pose primarily an inhalation hazard as opposed to direct exposure which is typical of gamma-beta emitters (e.g., Co-60, Cs-137) (Ref. 2).

The inhalation of TRU materials results in the deposit of radioisotopes in the lungs which can then be transported to, and deposited in, various organs throughout the body resulting in a long term committed dose. The combination of the highly energetic alpha particles (~5 MeV) and high specific activities can result in high committed doses for a very small uptake of material. For example, the inhalation of 1 µg of Pu-239 by a member of the general public would result in a dose of 37 mSv (3.7 rem) over a period of 50 years (Ref. 2). Since a single SWB is authorized to contain over 2000 grams of Pu-239 equivalent from a potential dose perspective (fissile gram equivalent is limited to 325

grams) (Ref. 3), the material contained within an SWB represents a very high potential dose consequence. Depending on the material form (e.g., solid, powder), chemical composition (e.g., elemental, oxide, hydride, nitride) and airborne release method (e.g., spill, fire) the release of the material in the SWB could result in exceeding the federal limit of 50 mSv (5 rem) per year for workers or 1 mSv (0.1 rem) for a member of the public while on a DOE site (Ref. 4).

Since inhalation of a very small amount of TRU materials can result in very high committed doses, combined with very long half-lives, TRU waste poses some unique challenges for proper storage, handling, and ultimate disposal. To help mitigate these challenges, a long term repository for TRU waste generated by the DOE has been established to minimize the potential impact of TRU waste on the public, workers, and the environment. For the DOE complex, this repository is the Waste Isolation Pilot Plant (WIPP) in Carlsbad, New Mexico (Ref. 1). In order to dispose TRU waste at the WIPP, the waste has to meet several criteria that have been established to ensure that the design basis of the WIPP is maintained, which includes (but is not limited to) heat generation, activity, fissile equivalent, weight, and size. The specific criteria that must be met are identified in the WIPP waste acceptance criteria (WAC) (Ref. 3).

To ensure that the fissile and activity content of TRU waste meets the WIPP WAC, an assay system certified in accordance with the WIPP quality criteria must be used (Ref. 3). One of these WIPP certified assay systems is the Super High Efficiency Neutron Counter (SuperHENC) (Ref. 5, 6). The SuperHENC uses both passive gamma spectroscopy as well as passive neutron detection to achieve WIPP certification (Ref. 5, 6). During the

counting process, the waste container is loaded into the assay chamber and is rotated, to give multiple angles for the gamma counting (Ref. 5, 6). Additionally, neutrons produced via spontaneous fission of Pu isotopes and Am-241 are counted to determine the equivalent amount of Pu-240 that is present (Ref. 5, 6). The gamma spectroscopy results are then fit to the observed fissile materials to produce an assay that meets WIPP's quality criteria (Ref. 5, 6).

While the SuperHENC assay provides assay data that meets WIPP's quality criteria, this process is expensive, and is therefore not generally used at DOE waste generation and staging locations until the waste is ready to be sent to WIPP for disposal. As a result, less sophisticated assay systems (such as the in-situ object counting system [ISOCS]) are used to provide assay data at DOE waste facilities prior to being sent to WIPP. This assay data is then used to establish and provide controls for the waste that are appropriate for the potential hazard they represent (Ref. 7).

If these assays are inaccurate it could result in either insufficient or excessive level of control for a given container of TRU waste. This is undesirable as it represents either a potential unsafe condition, or an unwarranted expenditure on control measures. In order to ensure that safety is maintained as efficiently as possible, it is desirable to ensure that the assays used in the field are capable of providing useful information regarding the contents of the containers that are as accurate as possible.

1.2   Source of Assay Data

Large quantities of equipment have been used for production and experimentation with

3

TRU isotopes. This equipment varies in size and composition, but can include large structures made of iron, aluminum, and copper based metals, as well as other associated materials including rubber, cellulose, and plastics (Appendix A). In the interest of minimizing disposal costs, large objects are decontaminated and reduced in size to the maximum extent practical.

Recently, a facility that had a number of oversized boxes (OSBs) which did not comply with the U.S. Department of Transportation (DOT) requirements for shipping over public roads underwent a size reduction campaign to place the contents of these OSBs into standard waste boxes (SWBs) that comply with DOT regulations (Figure-1, Appendix B).

The size reduction of the OSBs resulted in the generation of several SWBs. These SWBs were assayed using the ISOCS, a high purity germanium detector based system, to determine the amount and isotopes of TRU wastes present (Appendix A). This was accomplished by placing the ISOCS at a distance of approximately 6 ft from the SWB. This distance was chosen to ensure that the entirety of the SWB would fall within the solid angle of the detector (Figure-2). The ISOCS counted the resulting decay of TRU isotopes for approximately 30 minutes to ensure that good statistics were achieved. Depending on the SWB, a variety of TRU isotopes were detected. The predominate TRU isotope present was Pu-239, though others including Pu-238, Pu-240, Pu-241, Pu-242, and Am-241 were present in lesser mass quantities.
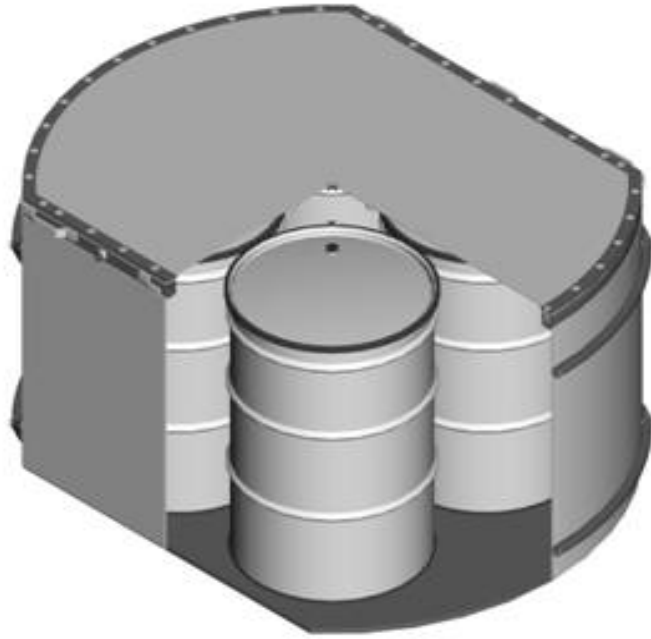
Figure-1: Standard Waste Box

The isotopic data generated by ISOCS for TRU wastes present within the SWB (Appendix A) was used by the facility to determine the potential dose consequences to the public and workers following a postulated release during an accident. The SWBs were subsequently sent to the Waste Isolation Pilot Plant (WIPP) for disposal. As part of the waste receipt process at the WIPP, the containers were assayed using the SuperHENC system (Appendix C). The values generated by the SuperHENC were, on average, higher than those identified by ISOCS (Appendix D). This generated a concern that ISOCS may not generate useful data for the estimation of accident consequences. This generated interest in determining if the method used to generate this data could be improved.

5

Figure-2: ISOCS Performing Assay on a Waste Container

1.3   Research Objectives

This thesis will investigate the capabilities and physical limitations of the ISOCS when used for the gamma spectroscopy of large containers. The specific objectives of this research are to determine if:

- Using the data available, the discrepancies between the SuperHENC and ISOCS assays can be explained

- ISOCS generates useful data when used for assay of SWBs

- The use of ISOCS can be improved to allow for better measurements in the future

The investigation of these topics will be pursued and presented in this thesis as follows:

Chapter 1   Introduction

This section discusses the background of the thesis and establishes the research objectives

Chapter 2   Review of Related Literature

This section discusses previous work on this topic and evaluates its applicability to the identified research objectives.

Chapter 3   Evaluation of Available Assay Data

This section evaluates the data that resulted from the assay of the SWBs using both the ISOCS and the SuperHENC systems. The evaluation will focus on the differences between these systems, and carry them forward for modeling and evaluation in the next section.

Chapter 4   Evaluation of the System using MCNPX

This section models the potential causes of the differences noted in Chapter 3. As additional information is gained from modeling the system, additional models will be developed to further clarify the underlying physics or the system.

Chapter 5   Integrated Discussion

This section integrates the discussions from the previous sections and establishes

www.manaraa.com

the overall findings of the research and potential additional issues that could impact these findings. The research objectives are then evaluated in the context of the findings of the research.

Chapter 6   Conclusions

This section states the conclusions reached with respect to the research objectives.

Chapter 7   Recommendations

This section identifies any potential topics for future research that would help clarify the physical processes and improve measurement using gamma spectroscopy.

Chapter 2 Review of Related Literature

Performing assays on large containers using only gamma spectroscopy is subject to several measurements uncertainties and system biases resulting from uncertainties in the matrix composition, self shielding, source distribution effects, and background irregularities (Ref. 8). Several methods have been identified to lower these uncertainties including both active and passive neutron counting (Ref. 8).

One such passive neutron counting solution is the SuperHENC. Several studies on the capabilities of the SuperHENC system have been performed (Ref. 5, 6, 9, and 10). SuperHENC was designed to address the assay issues inherent in larger containers such as SWBs (Ref. 5, 9, 10). These issues include the difficulties inherent in achieving precise measurements in some waste matrices as opposed to others, such as metals versus combustibles (Ref. 9). For example, high Z materials, such as iron can result in increased cosmic spalling as compared to lower Z materials, thereby elevating background radiation levels (Ref. 10).

Other challenges were associated with the SuperHENC being used for waste streams that could not be assumed to be primarily of a single waste profile (i.e., isotopic break down) or of a segregated waste type (i.e., metals, combustibles, plastics) (Ref. 10). To address these issues, validation testing of SuperHENC using a variety of configurations similar to wastes that are received at the WIPP has been performed (Ref. 6).

Although passive and active neutron counting systems have several advantages over gamma spectroscopy alone for accuracy, they are significantly more expensive (Ref. 8).

As a result, there is considerable interest in the use of gamma spectroscopy systems such as the ISOCS for in the field assay of radioactive contamination.

ISOCS has been used for the measurement of uranium and americium isotopes within the top 5 cm of contaminated top soil (Ref. 11). This soil contamination represents a distributed source through an essentially homogenous shielding material; however, it has significantly less depth than can be present within the SWBs (~175 cm, Appendix B). SWBs can also contain shielding materials with a higher density than soil. For example, iron, with a density of approximately 7.87 g/cm^3 may be present, while the top soil was identified as having a density of 1.3 g/cm^3.

Additionally, the presence of Pu isotopes in the top soil was inferred by a previously determined ratio of Am-241 to Pu-239 and Pu-240 (Ref. 11), rather than through direct measurement.

ISOCS has also been used to determine the surface contamination within sealed volumes, such as tanks and gloveboxes (Ref. 11). In these cases, the volumes were empty except for the surface contamination. These sealed volumes are similar to the SWBs, namely a solid metal container that has radioactive materials internally; however, the evaluated containers are empty, whereas the SWBs are filled with radioactive waste materials.

No literature was found that discussed the configurations present in the evaluated waste stream, namely the capabilities and physical limitation of ISOCS (or other similar gamma spectroscopy systems) to perform an assay of a large metal container (such as the SWB) that contains a distributed radioactive source.

Chapter 3 Evaluation of Available Assay Data

This section evaluates the data that resulted from the assay of the SWBs using both the ISOCS and the SuperHENC systems. This evaluation focuses on the differences between these systems, and identifies potential causes of these differences for evaluation through modeling using MCNPX in Chapter 4.

3.1   Comparison of SuperHENC data to ISOCS Data

The first step to determining if ISOCS was generating useful data was to compare the ISOCS data (Appendix A) to the data generated by SuperHENC (Appendix C). SuperHENC is a rigorously validated system for measuring isotopic constituents in TRU wastes that has been certified by WIPP as meeting its quality criteria (Ref. 1, 6, 9, and 10). WIPPs quality criteria for assay are considered the reference standard for TRU wastes within the DOE complex (Ref. 7).

As shown in Table-1, in the aggregate, all of the plutonium isotopes were measured as being in lower quantities by the ISOCS as compared to SuperHENC. Uncertainties are not listed for these values as, from the point of view of regulatory compliance, the assay data generated by ISOCS is significantly less than the SuperHENC data, and therefore even if the values were statistically the same, it would still be an unacceptable difference. It was also noted, however, that the offset, at this stage, did not appear to be consistent with a simple systematic bias, as there was great variation in the amount of offset between the two systems for the individual containers evaluated (see Appendix D). This disparity could have resulted from differences in how the two assay systems function on a

11

fundamental level.

Table-1: Aggregate Assay Data for SuperHENC and ISOCS

Isotope	SuperHENC (Ci)	ISOCS (Ci)	Difference (%)
Pu-238	6.02	2	-66.77
Pu-239	34.1	33.3	-2.34
Pu-240	9.88	8.33	-15.62
Pu-241	550	237	-56.92
Pu-242	3.84×10^{-3}	1.13×10^{-3}	-70.48
Am-241	22.6	55.5	146.19

The major difference between the two assays systems is that ISOCS detects only gammas emitted in the course of radioactive decay of the TRU isotopes, and uses only a single detector at a fixed location, while SuperHENC uses detection at multiple locations around the SWB for the gamma spectroscopy in conjunction with neutron detection.

Neutrons and gammas have significantly different attenuation factors for the materials present within the SWBs, which tend to be relatively high Z (Iron primarily), as compared to good neutron shields (such as water and plastics that are high in hydrogen). Since SuperHENC uses the neutron data in conjunction with the gamma spectroscopy data to determine the quantities of material present, it was likely that the combination of detector geometry as well as shielding composition within the SWB contributed to the observed discrepancies.

12

3.2   Evaluation of the Raw Data

In order to get a better understanding of the potential impacts of shielding on the accuracy of the ISOCS assay results, the raw detector data was evaluated. Since the primary isotope present within the SWBs was Pu-239 the evaluation focused on that isotope. Pu-239 is also advantageous as it has four distinct decay gammas (129.3, 203.55, 375.05, and 413.71 keV) that can be compared during shielding analysis.

The first step was to adjust for the efficiency of the detector. The detector efficiency was provided by the manufacturer in a calibration report (see excerpt from this report provided in Table-2 and Figure-3) (Ref. 12). The manufacturer's report identified a number of points of efficiency based on energy and angle of incidence. Although the curves are not, in general, straight lines, they were observed to be generally straight lines in the range of Pu-239 decay gamma energies, i.e., between 129.3 and 413.71 keV when plotted on a log-log graph.

Assuming that the curves are straight lines on the log-log chart in this region, the efficiencies at 0 and 90 degrees were interpolated for each of the Pu-239 decay gamma energies. Then, since the radioactive material is distributed throughout the containers, with the detector placed at an angle to the box to get as much of it within the solid angle of the detector, it was assumed to be reasonable to use a curve between the two lines shown in Figure-3 that is the average of the logarithm of the 0 and 90 degree efficiency values.

13

Table-2: ISOCS Detector Efficiency Values

E (keV)	0 deg.	1 sd %	90 deg.	1 sd %
30	2.21E-04	0.44	2.76E-07	31.60
60	2.50E-04	0.41	9.58E-06	2.47
90	2.49E-04	0.41	3.64E-05	1.22
122	2.36E-04	0.43	5.42E-05	0.98
344	8.27E-05	0.74	3.72E-05	1.19
662	3.85E-05	1.09	2.16E-05	1.56
779	3.21E-05	1.19	1.86E-05	1.68
1112	2.26E-05	1.42	1.39E-05	1.95
1408	1.71E-05	1.63	1.19E-05	2.09
2000	1.26E-05	1.91	9.30E-06	2.37
3000	7.47E-06	2.47	6.25E-06	2.88
5000	4.07E-06	3.34	3.20E-06	4.03
10000	1.16E-06	6.25	1.08E-06	6.93
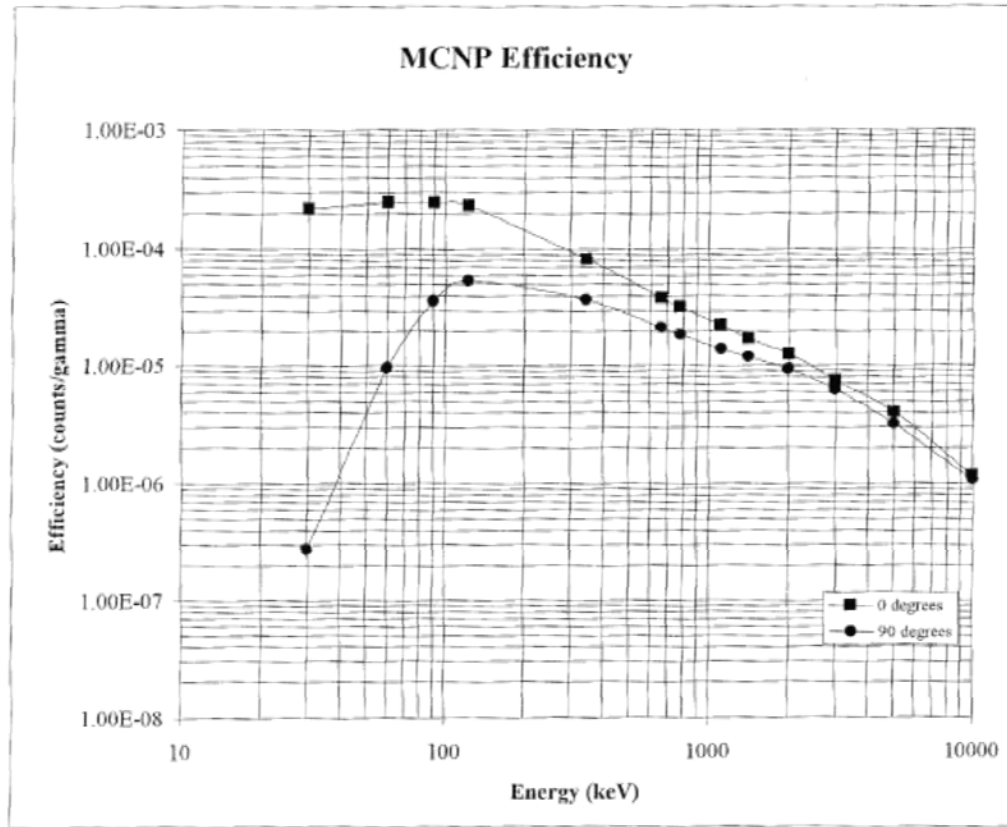
Figure-3: ISOCS Detector Efficiency Graph

While this could introduce some error in determining an absolute reading, it should be

14

noted that an inspection of the curve shows that the 0 and 90 degree efficiency lines are generally straight across the energies of interest (i.e., from 129.3 – 413.71 keV), with a generally consistent slope. As a result, any differences in the actual and assumed angle would result in an absolute, rather than a significant relative offset. Since the primary focus of the data analysis for this thesis is on the relative readings, any error introduced by a difference between the actual and assumed detector angles was not considered significant. For example, the average angle of incidence may be closer to 15-30 degrees; this would result in a systematic offset which should be relatively consistent across the data points. This also seemed appropriate, as the exact angle that the detector was placed with respect to the SWB is not known, and could not reasonably be expected to be placed with precision during the assay using ISOCS.

The second step was to normalize the data based on the relative intensity of the gammas during decay (decay branch ratios taken from BNL table of nuclides [Ref. 13]). The relative intensities for the Pu-239 decay gammas are shown in Table-3.

Using the detector efficiency and the gamma decay intensities, the raw data for a number of containers (see Appendix E for example data) was normalized, as shown in Table-4. The relative intensities of the peaks were normalized to 413.71 as it is the highest energy Pu-239 decay gamma.

This data was also graphed in Figure-4. Error bars are shown to illustrate the large range of potential values for the relative intensities, particularly for the weak 203.55 keV gamma energy.

Table-3: Relative Gamma Energy Intensity for Pu-239

Energy (keV)	Intensity (%)	Intensity (Relative)
129.3	6.31×10^{-3}	11.09
203.55	5.69×10^{-4}	1.00
375.05	1.55×10^{-3}	2.72
413.71	1.47×10^{-3}	2.58

Table-4: Relative Gamma Intensity for SWB Containers

Container	Energy (keV)	Relative Intensity	Uncertainty
NT060207R	129.3	0.354	25.93%
	375.05	0.946	10.55%
	413.71	1	15.01%
NT060208R	129.3	0.491	17.35%
	203.55	0.987	69.54%
	375.05	1.03	8.25%
	413.71	1	14.08%
NT060209R	129.3	0.403	1.56%
	203.55	0.619	5.85%
	375.05	1.02	2.60%
	413.71	1	2.74%

Table-4: Relative Gamma Intensity for SWB Containers (continued)

Container	Energy (keV)	Relative Intensity	Uncertainty
NT060210R	129.3	0.501	7.25%
	203.55	0.496	44.47%
	375.05	0.917	10.65%
	413.71	1	15.41%
NT060211R	129.3	0.284	3.12%
	203.55	0.534	10.82%
	375.05	0.919	4.35%
	413.71	1	5.79%
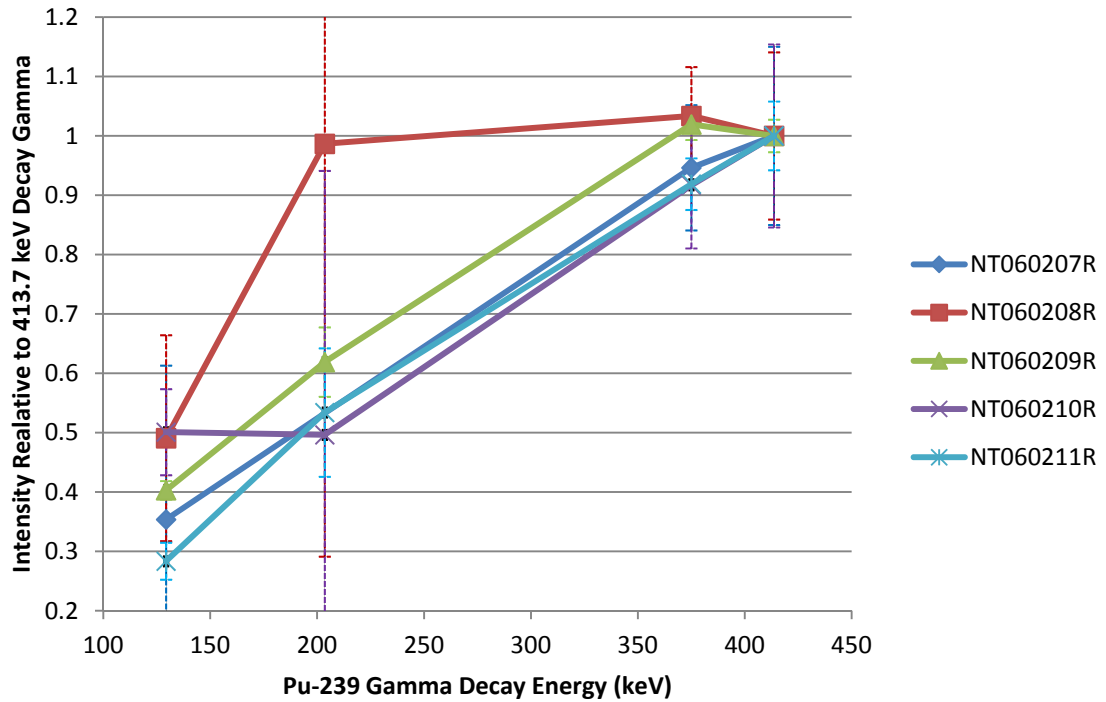
Figure-4: Relative Gamma Energy Intensity for Pu-239

3.3   Initial Method for Determination of Shielding Thickness

Using the normalized data for the SWBs, the following shielding equation (Ref. 14) was used to try to determine the amount of shielding present:

$$I = I_\circ e^{-\mu/\rho(\rho x)}$$

Where:

I = the shielded photon intensity

I_o = the initial photon intensity

μ/ρ = the mass attenuation coefficient

ρ = the density of the shielding medium [g/cm^3]

x = the thickness of the iron [cm]

Iron was used for this shielding determination, as it was the primary shielding material present within the SWBs (which themselves are primarily iron), with a nominal density of 7.87 g/cm^3. Using the values for mass attenuation for iron (Ref. 14) for selected photon energies, the mass attenuation coefficients for the Pu-239 decay gamma energies were linearly interpolated, as shown in Table-5.

Using the mass attenuation coefficient and the density of iron, arbitrary values for shielding thickness were plugged into the formula to see how they would impact the attenuation of the four Pu-239 decay gamma energies. It was observed that the greatest

attenuation occurs at lower energies, while higher energies are attenuated less.

Furthermore, this relationship is not constant, and the difference in attenuation for two

different shielding thicknesses becomes less at higher energies. Specifically, the

observed differences between the 413 and 375 keV peaks was quite small, which helps

explain why some of the data indicates lower normalized counts for the 413 peak as

compared to the 375 peak. This difference appears to fall within the range of uncertainty

of the measurements as shown in Figure-4.

Table-5: Mass Attenuation Coefficients for Iron
based on a Simple Weighted Average

Photon Energy (keV)	Mass Attenuation Coefficient	Source
100.0	0.344	Ref. 14
129.3	0.250	Interpolation
150.0	0.183	Ref. 14
200.0	0.138	Ref. 14
203.55	0.137	Interpolation
300.0	0.106	Ref. 14
375.05	0.095	Interpolation
400.00	0.092	Ref. 14
413.71	0.091	Interpolation
500.00	0.083	Ref. 14

Although the mass attenuation factors for a given gamma energy is constant, the

shielding present is being modified. By changing the shielding thickness, the intensity of

the radiation that can pass through the shielding material unattenuated is being reduced

19

logarithmically but at a different rate for the four energies being considered. As a result the intensity for the four different energies diverges depending on the thickness of the shielding present. Using this divergent nature of shielding for different energies, it should be possible to compare the observed normalized intensities to the calculated divergence to determine the amount of shielding present. To demonstrate this, a number of different shielding thicknesses of iron were postulated as shielding material for photons with the energies of gammas resulting from Pu-239 decay and plugged into the shielding equation discussed previously. The results and this calculation are presented in Table-6.

Table-6: Calculated Attenuation Factors for Pu-239 Decay Gammas in Iron
(Simple Weighted Average)

Shielding Thickness (cm)	Energy (keV)			
	129.3	203.55	375.05	413.71
0.25	0.73	0.91	0.99	1
0.5	0.53	0.83	0.98	1
1	0.29	0.7	0.96	1
2	0.08	0.48	0.93	1
	Attenuation Factor			

Table-6 shows that as the shielding thickness increases, the divergence of the normalized intensities will widen, as expected. By comparing the ratio between the 129.3 and 413.7 keV peaks it should be possible to determine the shielding thickness for a given shielding

20

material, in this case, iron. For example, if the ratio is found to be 0.35, it can be seen that this is between 0.5 and 1 cm of shielding thicknesses. By iteratively changing the value for thickness in the shielding equation between these two values, the thickness corresponding to a ratio between the 129.3 and 413.7 keV peaks of 0.35 can be found.

3.4   Application of the Initial Shielding Methodology

In order to apply this methodology to the SWBs, the available data set was reviewed to find SWBs that contained mostly iron based wastes. Six boxes were identified as containing greater than 90% iron, and an additional five boxes were identified as containing between 80% and 90%. Upon applying the shielding thickness determination methodology to these wastes boxes, an unexpected result was observed. By varying the assumed shielding thickness, such that, relative to the 413.71 keV gamma intensity that the 203.55 keV peaks were properly attenuated, the calculated value for 129.3 keV peaks were far less than the observed values.

For example, SWB NT060209R is identified as being composed of approximately 94.5% iron based metals. The normalized intensities for this SWB are shown in Table-7. At 1.5 mass attenuation lengths, the calculated values are as shown in Table-8.

As shown in Table-7 and Table-8, the calculated relative intensity for the 129.3 keV gamma is less than half that observed. In order to explore this further, the intensities relative to the 413.7 keV gamma were found for all the gamma peaks for the SWBs containing greater than 80% iron, and are presented in Table-9.

21

Table-7: Normalized Intensities for High Iron Content SWB

Energy (keV)	Relative Intensity	Uncertainty
129.3	0.40	1.56%
203.55	0.62	5.85%
375.05	1.02	2.60%
413.71	1	2.74%

Table-8: Calculated Intensities for 1.5 cm of Iron

	Energy (keV)			
	129.3	203.6	375.1	413.7
Relative Intensities	0.15	0.58	0.95	1

Table-9: Normalized Intensities for Several High Iron Content SWBs

Container	Energy (keV)	Relative Intensity	Uncertainty (%)	Intensity Relative to 413 keV peak	Calculated Shielding Thickness (cm)
Containers with > 90% Iron Contents					
NT060209R	129.3	0.4	1.56	0.4	0.75
	203.55	0.61	5.85	0.62	1.3
	375.05	1	2.60	1.02	-
	413.71	0.98	2.74	1	-

Table-9: Normalized Intensities for Several High Iron Content SWBs
(continued)

Container	Energy (keV)	Relative Intensity	Uncertainty (%)	Intensity Relative to 413 keV peak	Calculated Shielding Thickness (cm)
NT060211R	129.3	0.31	3.12	0.28	1.05
	203.55	0.58	10.82	0.53	1.75
	375.05	1	4.35	0.92	2.2
	413.71	1.09	5.79	1	-
NT070684R	129.3	0.4	4.16	0.35	0.85
	203.55	0.57	18.43	0.51	1.85
	375.05	1	10.05	0.89	3.1
	413.71	1.13	9.60	1	-
NT070685R	129.3	0.4	2.22	0.42	0.7
	203.55	0.66	8.04	0.69	1.05
	375.05	1	3.68	1.05	-
	413.71	0.95	5.34	1	-
NT070702R	129.3	0.33	2.84	0.32	0.9
	203.55	0.59	11.32	0.58	1.5
	375.05	1	4.38	0.99	0.3
	413.71	1.01	8.84	1	-

Table-9: Normalized Intensities for Several High Iron Content SWBs (continued)

Container	Energy (keV)	Relative Intensity	Uncertainty (%)	Intensity Relative to 413 keV peak	Calculated Shielding Thickness (cm)
NT070703R	129.3	0.42	2.08	0.4	0.75
	203.55	0.61	8.78	0.58	1.5
	375.05	1	3.56	0.95	1.4
	413.71	1.05	4.64	1	-
Containers with 80-90% Iron Contents					
NT070687R	129.3	0.42	3.22	0.43	0.65
	203.55	0.68	12.11	0.7	1
	375.05	1	5.32	1.04	-
	413.71	0.96	7.13	1	-
NT070692R	129.3	0.4	5.22	0.34	0.85
	203.55	0.61	22.62	0.51	1.85
	375.05	1	8.17	0.84	-
	413.71	1.2	14.97	1	-
NT070692R	129.3	0.35	1.40	0.35	0.85
	203.55	0.62	4.77	0.62	1.3
	375.05	1	2.15	1	-
	413.71	1	2.89	1	-

Table-9: Normalized Intensities for Several High Iron Content SWBs (continued)

Container	Energy (keV)	Relative Intensity	Uncertainty (%)	Intensity Relative to 413 keV peak	Calculated Shielding Thickness (cm)
NT070695R	129.3	0.38	1.83	0.37	0.8
	203.55	0.66	6.42	0.65	1.2
	375.05	1	2.95	0.99	0.3
	413.71	1.01	4.10	1	-
NT070700R	129.3	0.35	3.78	0.35	0.85
	203.55	0.57	15.74	0.56	1.6
	375.05	1	5.78	0.99	0.3
	413.71	1.01	8.53	1	-

As can be observed in the last column of Table-9, very diverse shielding thicknesses were determined based on the ratio of energies. For example, NT070702R shows thickness as 0.9 cm for 129.3 keV and as much as 1.5 cm for 203.55. This seems to indicate that the 129.3 keV gammas are being attenuated much less than they should be. It was considered that this could be the result of "buildup" of low energy gammas as a result of multiple attenuation events for higher energy gammas. This was believed at this point in the evaluation to be unlikely given the narrow energy peaks being considered, but was noted for future consideration. It was also noted for future consideration that this is a side effect of having a distributed source, rather than a point source.

Chapter 4 Evaluation of the System using MCNPX

In order to investigate the potential impacts of a distributed source suspended within a distributed shielding matrix, such as surface contamination on an iron substrate, a series of Monte Carlo Neutral Particle (MCNPX) models (Appendix F) were developed in accordance with the MCNPX manual (Ref. 15) to identify if the discrepancies between the actual ISOCS readings and the expected behavior based on the shielding equations were also present during modeling. Models included variations of both distributed and discrete sources within a shielding medium. In general, each model was an evolution of the previous models, and only those aspects that change between successive models are discussed. These models are discussed in detail in the following sections.

4.1 Evenly Distributed Source - Homogenous Shielding

The intent of this model was to determine the impact of a homogenous shielding material on a homogenously mixed source. The development of the model, results, and conclusions are discussed in the following sections.

4.1.1 Model: Evenly Distributed Source - Homogenous Shielding

The SWB was modeled as a simple rectangular box with wall thicknesses of 0.4 cm steel (98% iron, 2% carbon) based on typical characteristics of SWBs as identified by WIPP (Appendix B). Homogenous waste material was then added to the inside of the SWB.

The waste was modeled as a volumetric source with Pu-239 distributed through a shielding material with varying densities from 0.1 to 7.0 g/cm^3 consisting primarily of

26

iron, to approximate surface contamination on iron objects within the SWBs, consistent with the waste present in the SWBs that were assayed by ISOCS and SuperHENC, as shown in Figure-5.
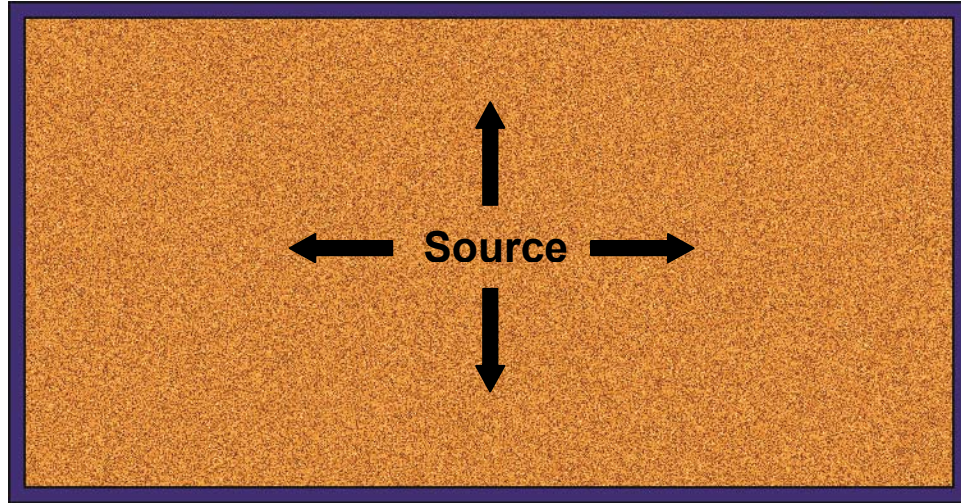
Figure-5: SWB Model with Evenly Distributed Source

Initially the detector was modeled as a small sized cylinder approximately 6 ft away from the SWB, consistent with the configuration of the actual measurements; however, initial modeling attempts were not successful. Specifically, very few photons were detected crossing through the detector, resulting in uncertainties that exceed the recommend values even with extended simulations (Ref. 16). As a result the model was modified to count photons escaping through one side of the box. The energies of these escaping photons were tallied so that there was a 1 keV range for the peak corresponding to the 4 primary decay gammas for Pu-239 (i.e., 129-130 keV, 203-204 keV, 375-376 keV, and 413-414 keV).

27

Additionally, it should be noted that the detector was modeled as a simple tally through the side of the SWB. This was advantageous as it isolates the behavior of the distributed source in the shielding matrix from possible interactions within the detector itself which may adversely impact the ability to determine the physical limitations of the system. In this regard, MCNPX provides a perfect detector, as it can count every photon that passes through a surface without attenuation or angular or energy sensitivities.

Counting all the photons that escape through one side of the box rather than simulating a detector at a distance similar to the actual ISOCS configuration was believed to be a reasonable approach for a number of reasons.

First, the evaluation is looking at the relative intensities to determine the shielding thickness. Relative intensities are based on the isotope undergoing radioactive decay and the attenuation between the source and the detector, not on the size of the detector. As a result, a larger detector will not impact the relative strengths of the photon peaks, and will significantly lower the statistical error resulting from a smaller detector size for a given number of photons.

Second, the discrepancies that were seen between calculated and observed values for the low energy photons were believed to be a result of the presence of a distributed source. As a result, removing the potential errors introduced by modeling another component in the system seemed prudent.

Third, several assumptions as to the composition of the SWBs have to be made to facilitate modeling. Additionally, the SWBs can vary greatly in terms of contents and

28

arrangements, so any assumptions made regarding the detector location and behavior are likely subsumed in the assumptions already made for the SWB contents.

The density of the shielding material was varied from a very low density (0.1 g/cm^3) to approximately the density of iron (7.0 g/cm^3). Initial runs were for 1 million photons, however, MCNPX identified statistical errors with this few a number of photons, and the photon count was increased to 100 million.

4.1.2 Results: Evenly Distributed Source - Homogenous Shielding

The results for the evenly distributed source with homogenous shielding model are presented in Table-10 and graphed in Figure-6 (normalized to 413.72 for direct comparison with the results presented from ISOCS). The maximum error identified for any of these points was 1.46% (the MCNP manual [Ref. 16] identifies that relative errors of less than 10% are reliable).

29

Table-10: Relative Intensities for Pu-239 Decay Gammas in a Homogenous Shield

		Gamma Energy (keV)			
		129.3	203.55	375.05	413.71
Shielding Density (g/cm³)	0.1	0.352	0.697	0.961	1
	0.5	0.258	0.610	0.946	1
	1	0.246	0.598	0.947	1
	1.25	0.243	0.592	0.944	1
	1.5	0.242	0.592	0.944	1
	1.75	0.241	0.591	0.944	1
	2	0.240	0.590	0.942	1
	2.5	0.240	0.591	0.939	1
	3	0.240	0.592	0.940	1
	3.5	0.239	0.592	0.937	1
	4	0.237	0.592	0.934	1
	5	0.238	0.595	0.939	1
	6	0.237	0.593	0.934	1
	7	0.238	0.589	0.935	1
		Normalized Intensity			
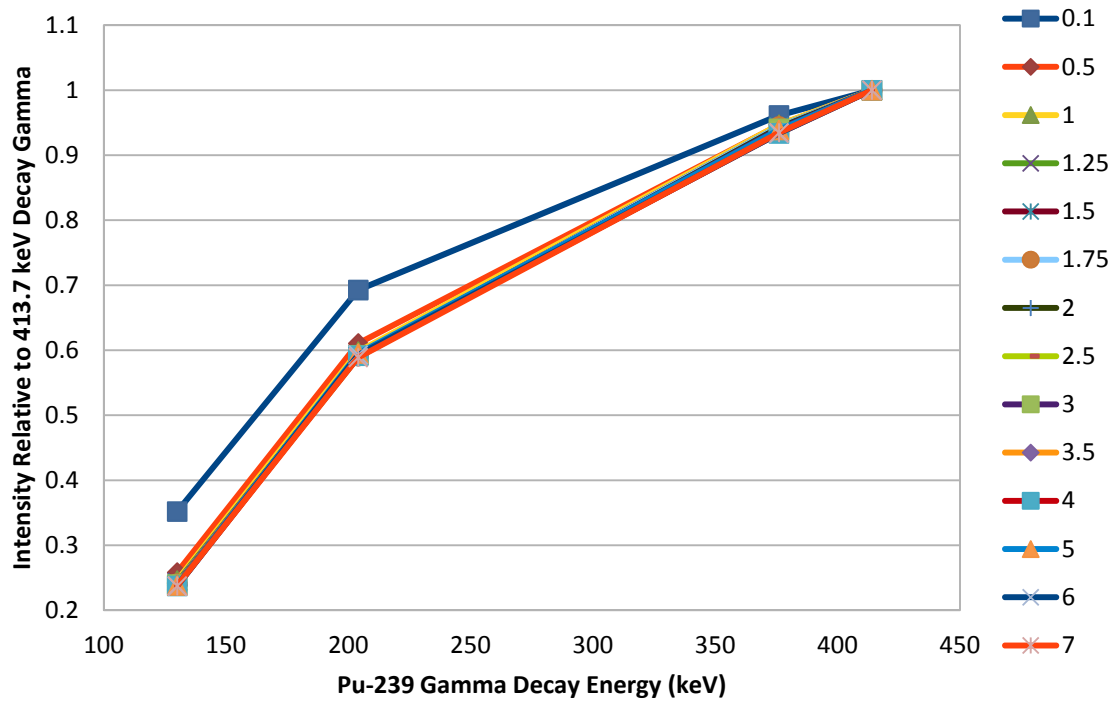
Figure-6: Relative Energy Frequency for Varying Shielding Density

4.1.3 Discussion: Evenly Distributed Source - Homogenous Shielding

These results were compared to the shielding equations to see if the same effect that was seen for the ISOCS assay data was replicated in MCNP, namely an increased number of low energy photons as compared to those predicted by shielding equations.

This comparison focused on matching the calculated shielding thicknesses to the MCNP results in the 1 to 2 g/cm^3 range. First, the gamma abundance was normalized to the highest energy (413 keV). Then the assumed shielding thickness was varied until the normalized intensity for the 203 keV gamma peak matched that shown in MCNP. Initially, this produced around 16.3% for the 129 keV based on the calculated values

31

using the shielding equation and 24.6% for the MCNP values.

At this point it was acknowledged that some error may have resulted from using a simple weighted average to determine the mass attenuation coefficient (Figure-7). It had been necessary to interpolate the constant, as there were no available sources that had the mass attenuation coefficients for the specific gamma energies of interest. A weighted average of the logarithm of the mass attenuation coefficients produced a much smoother curve (Figure-8) and is believed to be a better approximation of the actual mass attenuation coefficients as compared to the simple weighted average (Figure-7). Specifically, the value for mass attenuation at 129.3 keV produces a much smoother curve in relation to the surrounding points for the weighted average of the logarithmic values as compared to a simple weighted average.
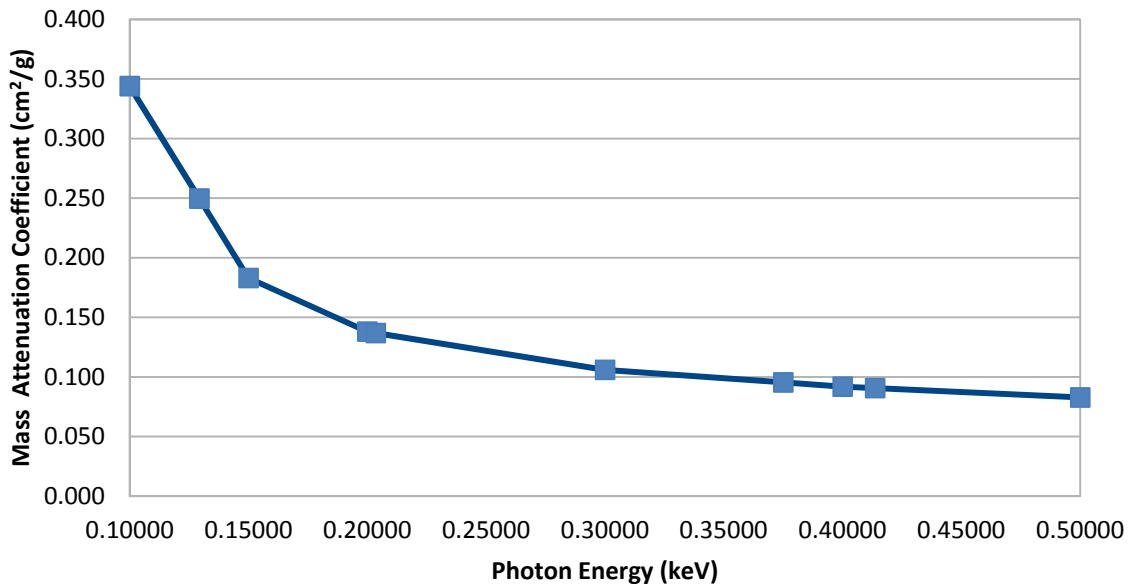
Figure-7: Mass Attenuation Coefficients (Simple Weighted Average)
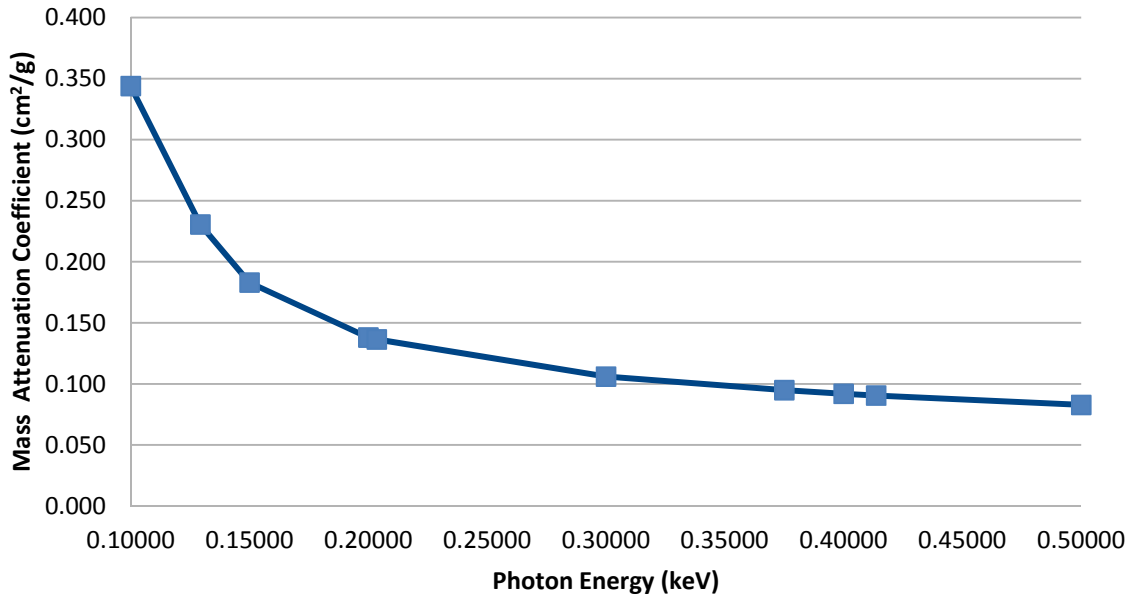
Figure-8: Mass Attenuation Coefficients

(Weighted Average of Logarithmic Values)

The values that resulted from the weighted average of the logarithmic values of the mass attenuation coefficients are shown in Table-11.

By using the values obtain from the weighted average of the logarithmic values (Table-11), the calculated value for the 129 keV gamma increased to 20.1% versus 24.6% for the MCNP values. It was noted, that this is still a difference of 22% in abundance, which is significant when compared to the identified error of 1.46% relative to the measured values. Relative attenuations based on the weighted average of the logarithmic values of the mass attenuation coefficients are provided in Table-12.

33

Table-11: Mass Attenuation Coefficients for Iron
Based on the Weighted Average of the Logarithmic Values

Photon Energy (keV)	Mass Attenuation Coefficient	Source
100.0	0.344	Ref. 14
129.3	0.231	Interpolation
150.0	0.183	Ref. 14
200.0	0.138	Ref. 14
203.55	0.136	Interpolation
300.0	0.106	Ref. 14
375.05	0.095	Interpolation
400.00	0.092	Ref. 14
413.71	0.090	Interpolation
500.00	0.083	Ref. 14

Table-12: Calculated Attenuation Factors for Pu-239 Decay Gammas in Iron
(Weighted Average of the Logarithmic Values)

		Energy (keV)			
		129.3	203.55	375.05	413.71
	0.25	0.76	0.91	0.99	1
Shielding Thickness (cm)	0.5	0.57	0.83	0.98	1
	1	0.33	0.7	0.96	1
	2	0.11	0.48	0.92	1
		Attenuation Factor			

34

It was also acknowledged that buildup of photons at lower energies (~100 keV) as a result of the Photo Electric Effect and Compton Scattering of higher energy photons could introduce error resulting in the observed discrepancies. For example, it was possible that the amount of low energy photons had built up to the point where the 129.3 keV peak was indistinguishable from the background of attenuated photons.

To investigate if buildup of low energy photons was occurring, additional MCNPX models were run using the same parameters as previously (i.e., same number of photons, with identical source at 1 g/cm^3 shielding density), but with an additional 1 keV wide tally on either side of the tally for the 129 keV. The results of this modeling are shown in Table-13:

Table-13: Relative Gamma Intensity in the Vicinity of the 129 keV Peak

Energy Bin (max keV)	Intensity	Relative Error (%)
128	1.344×10^{-3}	0.27
129	5.138×10^{-5}	1.40
130	1.421×10^{-3}	0.27
131	1.419×10^{-5}	2.65

The peak for the 129 keV gamma is 27 times that of the next lower bin, and 100 times larger than the next higher one. This (and the error as reported by MCNP) indicates that the cause of the elevated photons in the 129-130 energy bin is not the result of buildup.

The higher than expected ratio between low energy and high energy photons could have

been caused by the presence of a distributed source in a shielding matrix. For example, if only one locality is considered, more unattenuated 413.7 keV Pu-239 decay gammas should arrive at the detector from that locality than unattenuated 129.3 keV Pu-239 decay gammas, once normalized for decay intensity (Table-3), as a result of differences in attenuation based on photon energy (Table-6). On the other hand, if a second locality, closer to the detector is postulated, a higher fraction of the 129.3 keV gammas relative to the 413.7 keV gammas would arrive at the detector. Taken separately, the total amount of shielding between the source and the detector could be found using the calculated value, however, if both are present, the shielding thickness is harder to determine.

In this example, suppose the two sources are of equal strength are on a straight line along the axis of the detector, with one source being at 0.5 cm of shielding distance and the second at 1.0 cm for 129.3 keV . Based on Table-12, the 129.3 keV gammas would be at an intensity of 0.57 and 0.33 relative to the 413.7 keV peak for 0.5 cm and 1.0 cm respectively.

It must be considered, however, that the 413.7 keV gammas are also attenuated through that distance. If the unshielded intensity of both sources is assumed to be 1, the intensity of 413.7 keV gammas would be 0.702 and 0.492 for shielding thicknesses of 0.5 cm and 1.0 cm respectively. This would result in a shielded relative intensity of 129.3 keV gammas of 0.400 and 0.162 for shielding thicknesses of 0.5 cm and 1.0 cm respectively.

Adding these two sets together results in an intensity of 1.194 for 413.7 keV gammas and 0.562 for 129.3 keV gammas. Normalizing these values to 413.7 results in a relative intensity of 0.471 for the 129.3 keV gammas.

36

By iteratively applying the shielding equations to solve for a relative intensity of 0.471 for 129.3 keV gammas, a shielding thickness of 0.678 cm is found. Based on a shielding thickness of 0.678 cm, the intensity of 413.7 keV gammas should have fallen off by a factor of 0.619 from the original intensity. Based on the intensity of 1.194 identified above and the shielding present would result in a combined source intensity of 1.92. Since we started with two sources each with an intensity of 1, the impact of the multiple sources on the perceived relative intensities and associated shielding thickness result in a 4% underestimation of the actual source strengths.

It is also interesting to note that the curves identified in Figure-6 appear to rapidly converge on one value. This behavior was also not anticipated by application of the shielding equation (Table-12). As density increases, it was expected that the ratio of lower to higher energy photons intensities would continue to decrease. Since the system does not appear to be saturated with low energy photons (as shown in Table-13), it is postulated this is another result of having a distributed source in a shielding matrix. The impact of increasing shielding matrix density on the ratio of photon intensities will be investigated further.

4.2   Localized Distributed Source - Homogenous Shielding

The intent of this model was to determine the impact of a localizing the shielding at one end of the SWB or the other would result in the behavior that would be expected based on the shielding equations. The development of the model, results, and conclusions are discussed in the following sections.

4.2.1   Model: Localized Distributed Source - Homogenous Shielding

Initially an evenly distributed source throughout the SWB was modeled, while varying the shielding material density (as per Section 4.1.1). Subsequently the source was modeled as a Gaussian distribution concentrated at either end of the SWB (as shown in Figure-9), while maintaining the same source strength and varying the shielding material density. All three of these models were run in two different configurations that included or excluded the shielding provided by the SWB itself.
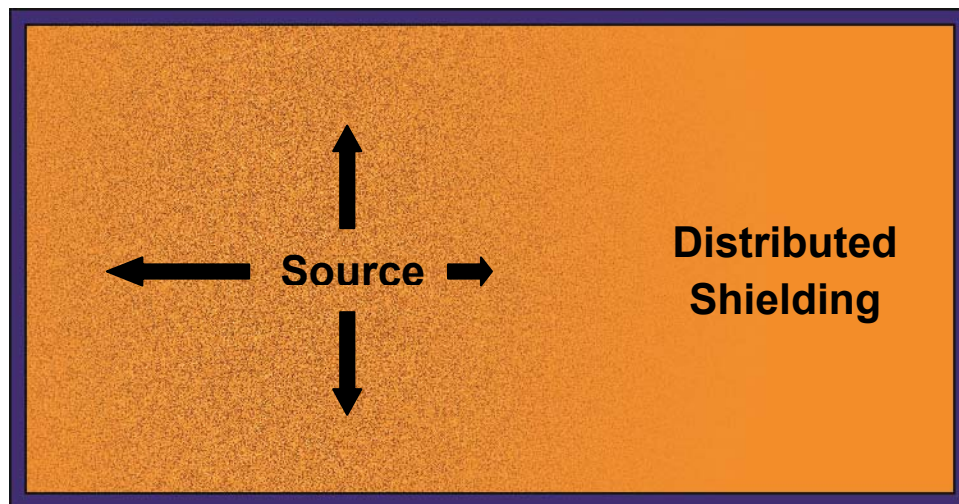
Figure-9: SWB Model with Localized Distributed Source

4.2.2 Results: Localized Distributed Source - Homogenous Shielding

The results of modeling a locally distributed source throughout a homogenous shielding material are shown in Figure-10. The maximum error identified for any of these points was 1.95%.

The upper set of lines represent the model without the SWB present, with the source near the detector (NBNS), evenly distributed (NBDS), and far from the detector (NBFS). Similarly, the lower set of lines represent the model with the SWB present, with the source near the detector (BNS), evenly distributed (BDS), and far from the detector (BFS). As can be seen, the ratio between 129.3 and 413.7 keV peaks became asymptotic, approaching a single value at higher shielding thicknesses.
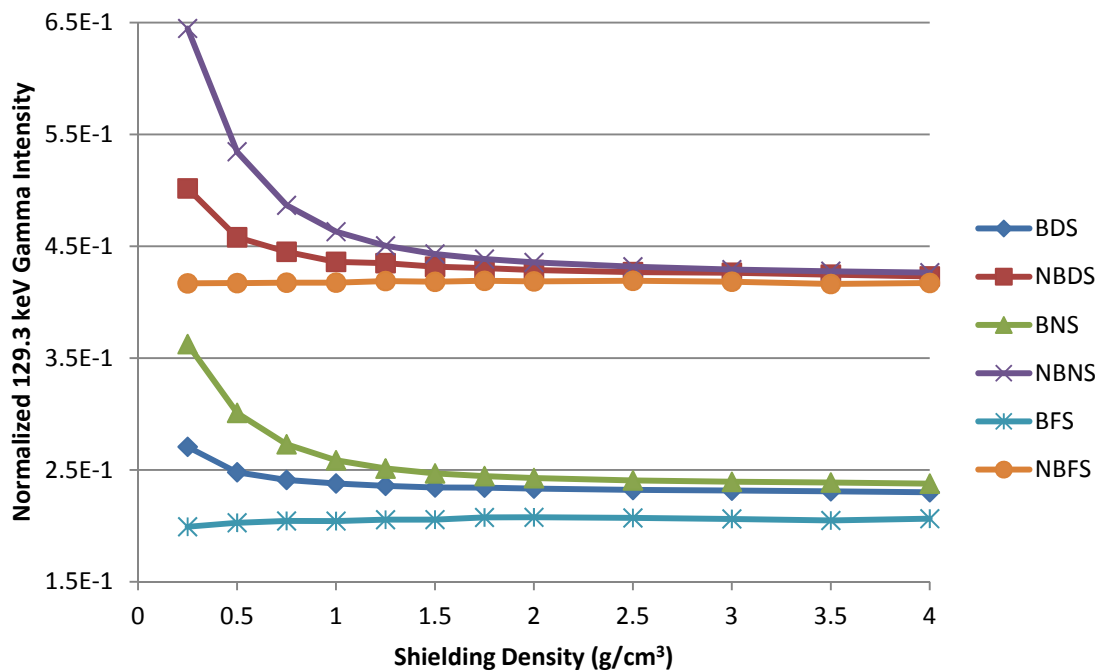
Figure-10: Modeling of Evenly and Locally Distributed Sources

4.2.3 Discussion: Localized Distributed Source - Homogenous Shielding

As previously discussed in Section 3.3, the ratio between the intensities for Pu-239 decay gammas should be an indicator of the shielding present between the source and the detector. However, an examination of Figure-10 indicates that this may not work for a distributed source.

Specifically, it is observed the ratio of lower to higher energy photons intensities appears to converge once a certain shielding thickness is present. This is contrary to the behavior anticipated by the shielding equations (Table-12) namely that the ratio should continue to decrease logarithmically. It is also observed that the presence or absence of the SWB in the model appears to have the primary effect of shifting the entire curve, rather than greatly changing its shape, though it is noted that the presence of the SWB appears to flatten the extremes of the curve.

To verify that the convergence is not caused by buildup of low energy photons, the energy bins next to the 129.3 keV gamma peak were examined to see if there was evidence of significant buildup as shown in Table-14. The energy bin containing the 129 keV gamma is 17 times that of the next lower bin, and 48 times larger than the next higher one, indicating that buildup of low energy photons does not have a significant impact on the results of this model.

Table-14: Relative Photon Intensity in the Vicinity of the 129 keV Peak - 4 g/cm^3 Far Source with SWB Model

Energy Bin (max keV)	Intensity	Relative Error (%)
128	2.273×10^{-4}	0.68
129	5.780×10^{-6}	4.16
130	1.079×10^{-4}	0.96
131	2.260×10^{-6}	6.65

It was possible that these results were impacted by the distributed source being only roughly defined within the shielding matrix, and therefore additional modeling using a distributed source with clearly defined boundaries seemed appropriate.

4.3 Fixed Volume Distributed Source - Homogenous Shielding

The intent of this model was to establish a source with consistent properties, namely strength and dimensions, to further explore the potential impact of a homogenous shielding material on a distributed source. The development of the model, results, and conclusions are discussed in the following sections.

4.3.1 Model: Fixed Volume Distributed Source - Homogenous Shielding

To ensure that the observed results were not a product of slight differences in the distribution of the source, the source was then modeled as a fixed volume. Specifically, a volumetric source was modeled that extended the width and height of an SWB but was only 40 cm long, as shown in Figure-11. To help isolated the effect of the distributed shielding on the system, the SWB was not included in the model.

The fixed volume was moved through the distributed shielding material, starting at one end of the material then moving to the far side. As before, the shielding material density was varied for each source location.

42
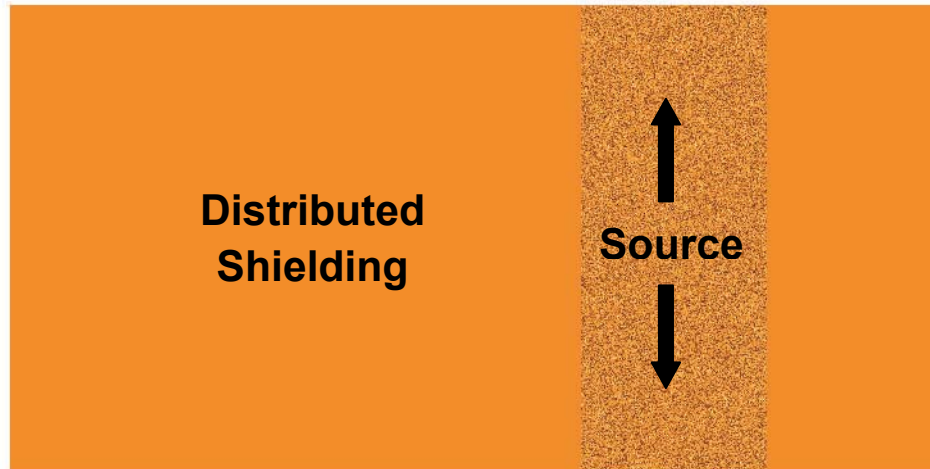
Figure-11: SWB Model with Fixed Volume Distributed Source

4.3.2   Results: Fixed Volume Distributed Source - Homogenous Shielding

The results of the modeling of a fixed volume distributed source being moved through a homogenous shielding material are shown in Figure-12. The maximum error identified for any of these points was 0.96%.

It was observed that once the source is moved past the middle of the SWB, all the lines converge. Additionally, as the shielding density increases, the lines for the closer sources appear to be converging on the lines for those further from the detector, with those closer to the detector taking large amounts of shielding density to approach the results of from the more distant sources.

43
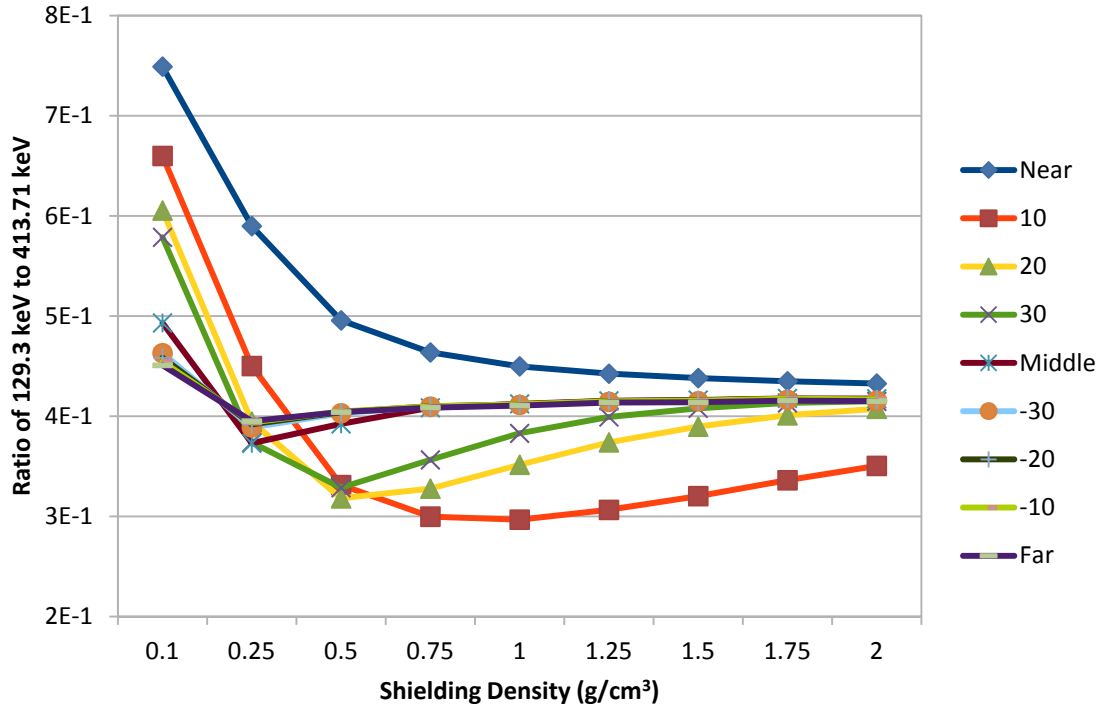
Figure-12: Results for a fixed volume source moved throughout the container

4.3.3   Discussion: Fixed Volume Distributed Source - Homogenous Shielding

It is worth noting that as the source moved closer to the far end of the SWB, it became the same configuration as with the source on the near end, except with the detector reversed. For example, the configuration with the source 10 cm from the far end of the SWB is the same as 10 cm from the near end, with the detector on the opposite side.

It is interesting that the results (Figure-12) indicate that the attenuation of 129.3 keV photons relative to 413.7 keV photons appears to initially decrease with increased shielding thickness consistent with the expectations of the application of the shielding equation (Table-6) but then increase. This increase of 129.3 keV photons relative to

44

413.7 keV photons appears consistent with the observed results from the actual data (Section 4.1.2). This could be caused be either geometry effects on distributed sources as discusses in Sections 4.1.3 and 4.2.3, or buildup of 129.3 keV photons resulting from attenuation of higher energy photons.

To determine if buildup of low energy photons was causing the observed increase in low energy photons, the energy bins next to the 129.3 keV gamma peak for the source modeled at 10 cm away from the detector were evaluated as shown in Table-14. This case was chosen because it showed the greatest trend of increasing ratio between high and low energy photons as shown in Figure-12.

The energy bin containing the 129 keV gamma is 41 times that of the next lower bin, and 106 times larger than the next higher one, indicating that buildup of low energy photons does not have a significant impact on the results of this model and is therefore not the cause of the upward trend in low energy photons relative to higher energy ones.

Table-15: Relative Photon Intensity in the Vicinity of the 129 keV Peak - 2 g/cm^3 Source 10 cm from detector

Energy Bin (max keV)	Intensity	Relative Error (%)
128	2.802×10^{-3}	0.19
129	7.387×10^{-5}	1.16
130	3.060×10^{-3}	0.18
131	2.886×10^{-5}	1.86

At this point, it was also noticed that the ratio between 129.3 and 413.7 keV photons

appears to be converging on a value around 0.416. Similar values are also present in previous simulations where the SWB was not included in the model (Section 4.2.2). As can be seen in Figure-10, the results from that model, without the SWB converged around 0.42.

It is unclear what the significance of this value might be. It is possible that this is related to the mean free path of photons within the distributed shielding material. Mean free path is the inverse of the of μ value defined in the shielding equation in Section 3.3.

Using the shielding equation, it can be determined that a relative attenuation ratio of 0.42 between 129.3 and 413.7 keV photons corresponds to approximately 6.1 cm of iron shielding. This in turn corresponds to approximately 1.4 mean free paths for 129.3 keV photons and 0.55 mean free path lengths for 413.7 keV photons. However, it is not immediately clear what the significance of these mean free path lengths might be, although it is noted that the 129.3 keV photons are traveling through approximately one mean free path more than the 413.7 keV in this distance.

As shown in Figure-6, the relative attenuation appears for other energies also appear to stabilize at a given value. This effect may warrant additional research. However, the determination of the significance of the ratio of mean free paths at the point of convergence, while interesting, does not seem to directly impact the research objectives, other than to acknowledge that it places a limit on the attenuation of low energy photons in a distributed source as compared to high energy photons.

In order to determine if these observations held in the case of a more complex source, the

46

next step was to evaluate a SWB model with several sources with different densities placed within a shielding matrix. Additionally, it would be of interest to determine the impact of multiple detector locations on the results.

4.4   Complex Source

The intent of this model was to determine if the presence of a number of discrete sources within a homogenous inter-source shielding matrix would provide results similar to those seen for a homogeneous mixture of TRU waste materials within an SWB. The development of the model, results, and conclusions are discussed in the following sections.

4.4.1   Model: Complex Source

This SWB model included multiple discrete sources with different densities within a homogeneously mixed inter-source shielding as shown in Figure-13. The model was then modified to include a tally across every box surface, i.e., the top, bottom, left, right, front, and back surfaces of the box.

Figure-13: SWB Model with Complex Sources

4.4.2 Results: Complex Source

Initial results showed large errors at 100 million photons, so the model was modified to increase the number of photons to 1 billion. This reduced the error to a maximum error of 7.76% for all the points for 1 g/cm^3 or less. The error for points beyond 1 g/cm^3 continued to increase but were included in the results to show the general trends. The results are shown in Figure-14.
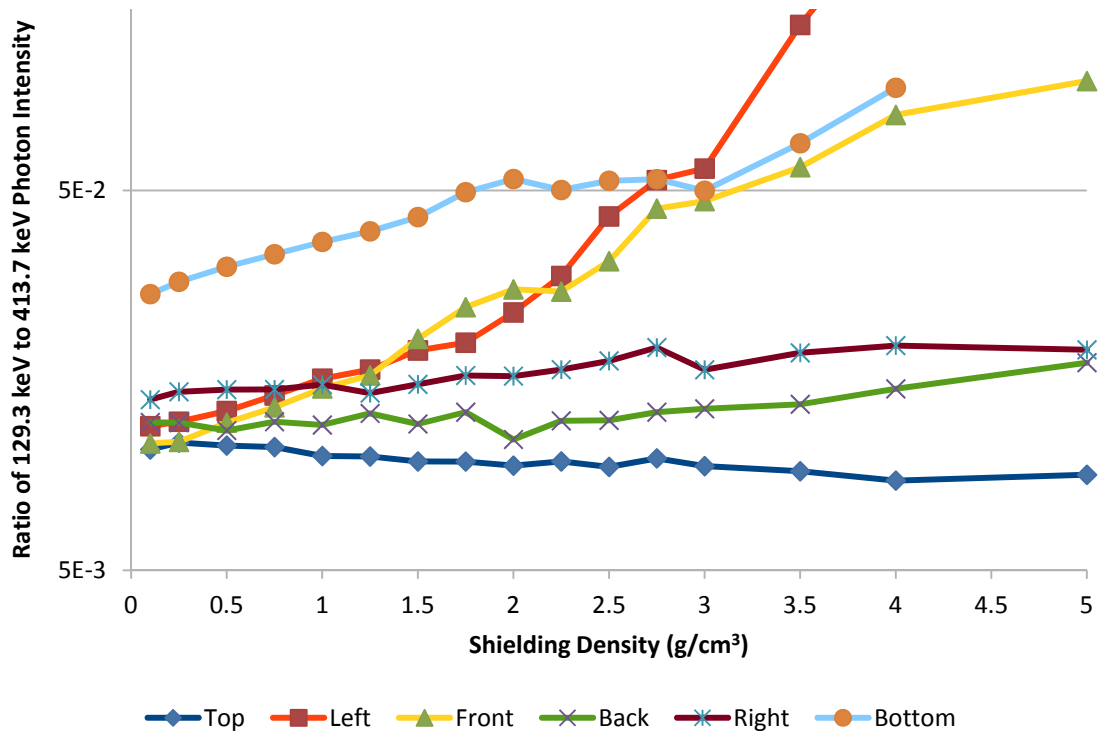
Figure-14: Results for SWB Model with Complex Sources

4.4.3 Discussion: Complex Source

Results at low densities of the inter-source shielding (0.01 – 1.0 g/cm^3) were general consistent with the observations in Section 4.3.3, namely that the ratio between low and

high energy photons tend to converge.

At higher densities (2.0-5.0 g/cm^3), however, it became clear that the ratios between high and low energy photons were diverging instead of converging. At this point it was noticed that the 1 keV bin on either side of the 129.3 keV spectrum lines were almost the same value as the energy bin for the actual peak. An example is provided for the bottom SWB surface tally in Table-16. The maximum error identified for any of these points was 2.39%.

Table-16: Relative Intensities for Low-Energy Photons for the Bottom Tally

		Inter-Source Shielding Density (g/cm^3)			
		0.1	0.25	0.5	0.75
Maximum Energy (keV)	129	1.35x10^{-5}	8.23x10^{-6}	3.75x10^{-6}	1.79x10^{-6}
	130	1.40x10^{-5}	8.12x10^{-6}	3.63x10^{-6}	1.75x10^{-6}
	131	1.34x10^{-5}	8.05x10^{-6}	3.63x10^{-6}	1.75x10^{-6}
Ratio of 130 to 129		1.03	0.987	0.968	0.980
Ratio of 130 to 131		1.04	1.01	1.00	1.00

The very low ratios (~1) between the three bins indicates that the majority of the counts detected in the 129-130 keV bin were from photoelectric effect and Compton scattering interactions with photons that were born at higher energies, namely the 413.7, 375.1, and 203.6 keV Pu-239 gamma peaks. This is contrary to what had been seen for the homogenous mixtures seen the previous models (Table-13, Table-14, Table-15). This is likely the result of transitioning from a source with a homogenous source distribution to a

model with more complex and dense sources.

It was acknowledged at this point that the shielding density that was being modeled exceeded the actual density that could be present. Although this does not change the physics of what is occurring within the SWB, it does illustrate that although a general solution to this issue may not be available, a solution for the specific parameters of interest might be.

For example, it would not be possible to determine the source strength within an SWB that had infinite shielding, as none of the photons would escape. This would be true if the source was small, or extremely large, unless the source itself was infinite. As a result, there will always be some limit to what can be determined with a given source, shielding thickness, and detection capability.

Two potential paths forward were identified at this point, both of which were pursued and discussed in the following sections. The first is to isolate the photon energies, to confirm that the photons observed in the 129-130 keV range are, in fact, originating at the higher energy peaks (see Section 4.5). The second is to reduce the density of the complex sources to see if useful results can be observed using SWBs with nominal masses consistent with what can be accepted at the WIPP (see Section 4.6).

4.5 Complex Source – Mono Energetic

This model was intended to allow for isolation of specific energy peaks to determine how many high energy photons eventually result in energies that are in the lower energy bins that are being evaluated. The development of the model, results, and conclusions are discussed in the following sections.

4.5.1 *Model: Complex Source – Mono Energetic*

In order to determine if the photons being observed in the 129-130 keV energy bin were resulting from photons being born at the higher energies of 203.6, 375.1, and 413.7 keV, the MCNPX model was modified to include only one energy at a time. Specifically, the model was run at 413.7 and 129.3 keV. To ensure that error was kept within the recommend error range (Ref. 16), the number of photons modeled was adjusted to 10 billion, with all of these photons originating at a single energy. Other than these changes, the model was identical to those used previously (See Figure-13).

4.5.2 *Results: Complex Source – Mono Energetic*

The results from the monoenergetic model are presented in Figure-15, which also includes the results from the polyenergetic model for comparison. The maximum error identified for any of the 413.7 keV points was 0.57%. Even at 1 billion photons, the error for the 129.3 keV was considerably higher at an average of 46.8% for the 0.75 g/cm^3 points. The number of runs was raised to 10 billion for a few points, such at the 0.50 g/cm^3 point, which reduced the error to a maximum of 17.7% and an average of 8.5%.

52

However, as noted in Section 4.4.3, the density of the system exceeds that allowed for SWBs so limited value was seen in doing additional runs at 10 billion photons considering the time frames involved, and that at this point, all that was need was a rough approximation of the value for comparison purposes.

These results were graphed using a logarithmic axis for the ratios to allow the monoenergetic and polyenergetic results to be easily compared. The data showed a trend for the polyenergetic ratio to be mostly flat at the evaluated densities, but increasing slightly. The monoenergetic ratio showed a tendency for the ratio to decrease as shielding density increased.
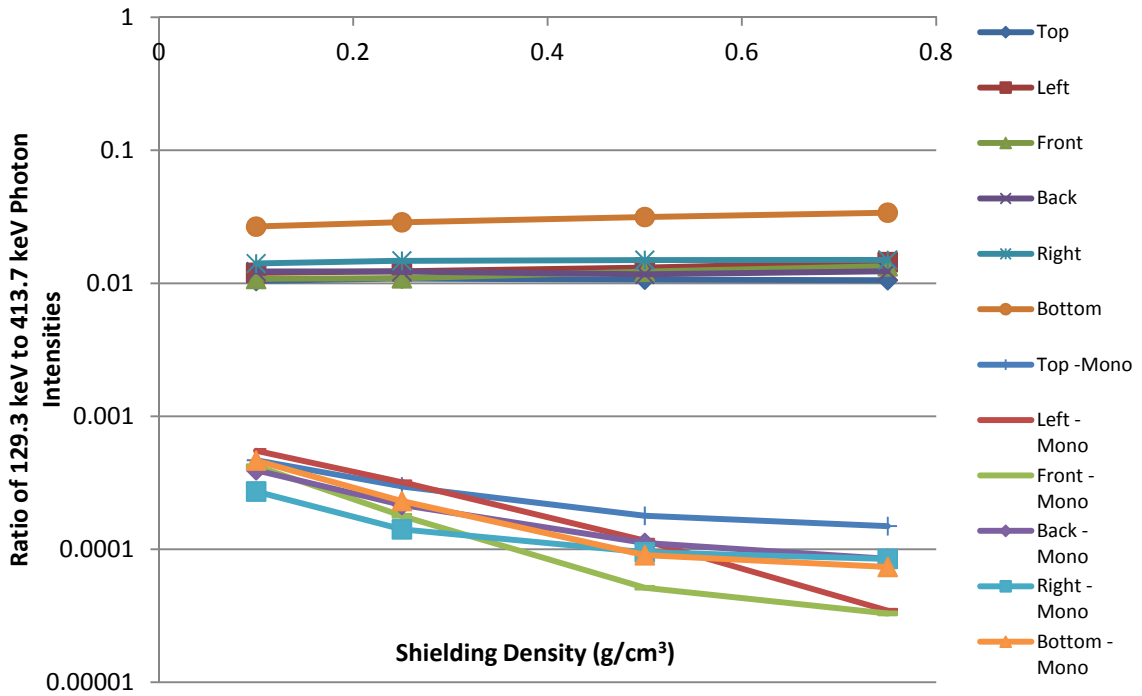
Figure-15: Ratio of Photon Intensity in Monoenergetic and Polyenergetic Sources

The number of photons that originated at 413.7 keV that were detected within the

413-414 keV bin were compared to the number of photons in the 129-130 keV bin, when only 413.7 keV source photons were present (monoenergetic). This was then compared to the ratio between the 413-414 keV and the 129-130 keV bin when all the energies were present (polyenergetic). The maximum error for any of the values considered in this comparison was 3.19% for the monoenergetic values and 6.18% for the polyenergetic values. The results are shown in Table-17.

Table-17: Percentage of Low Energy Photons Born at Higher Energies

Detector Location	Inter-Source Shielding Density (g/cm^3)			
	0.1	0.25	0.5	0.75
Bottom	51.07%	53.60%	55.15%	56.22%
Top	49.17%	50.73%	52.12%	51.90%
Back	48.23%	52.84%	57.28%	56.46%
Left	48.14%	49.92%	51.22%	52.14%
Front	50.31%	54.83%	56.05%	56.03%
Right	49.81%	53.46%	55.47%	57.04%
	Percentage of Polyenergetic 129-130 keV photons born at 413.7 keV			

4.5.3   Discussion: Complex Source – Mono Energetic

The monoenergetic model confirms the conclusions of Section 4.4.3, namely that the modeling of the complex source combined with the inter-source shielding thicknesses results in a very poor differentiation between the 129.3 keV peak resulting from

54

unattenuated flux from the source as compared to attenuated flux being born at higher energies. This is shown in the data as presented in Figure-15, which shows that the ratio between 129.3 and 413.7 keV photon intensity in the monoenergetic case is two orders of magnitude lower than in the polyenergetic case. This is confirmed in Table-17 which shows that around half of the total 129-130 keV photons in the polyenergetic case are born at 413.7 keV. With the addition of 129-130 keV born at either 203.6 or 375.1 keV, the number of photons born at 129.3 that arrive at the detector unattenuated is a minor contributor to the whole.

It was considered that the width of the energy band could be narrowed to isolate the unattenuated flux peak (e.g., 129.29 to 129.31). This approach was rejected, however, as it is not believed, based on the data provided, that ISOCS would be able to discriminate to this level of precision, even if MCNPX can. This is consistent with the peak widths shown in Appendix A that are typically 2 keV wide at full width half maximum (FWHM).

As a result, the next step was to reduce the evaluated densities to be more consistent with those that are actually present in SWBs. If the signal-to-noise ratio observed for the complex source as discussed in this section and in Section 4.4.3 continue, then it may indicate that for bulky objects, such as the SWBs, the ISOCS is inadequate for performing accurate assays.

4.6   Complex Source – Reduced Density

The intent of this model was to reduce the density of shielding materials within the SWB to quantities that are more representative of the conditions that were present during the actual measurements. The development of the model, results, and conclusions are discussed in the following sections.

4.6.1   Model: Complex Source – Reduced Density

The model developed in Section 4.4.1 was modified to reduce the densities of the discrete sources by about a factor of 4, as shown in Figure-16. Additionally, the density of the distributed shielding was only evaluated up to 0.75 g/cm^3.

This value was based on the maximum allowed weight of the contents of an SWB of 3,360 pounds, which converts to approximately 1,527 kg (Appendix B). The inside dimensions of the SWB are 36 9/16" x 68 3/4" x 52", which converts to roughly 93cm x 175 cm x 132 cm for a volume of 2,148,300 cm^3 (Appendix B). Given the maximum mass of 1,527 kg and the volume, the maximum allowed density is approximately 0.71 g/cm^3.

56

Figure-16: SWB Model with Reduced Density Complex Sources

4.6.2 Results: Complex Source – Reduced Density
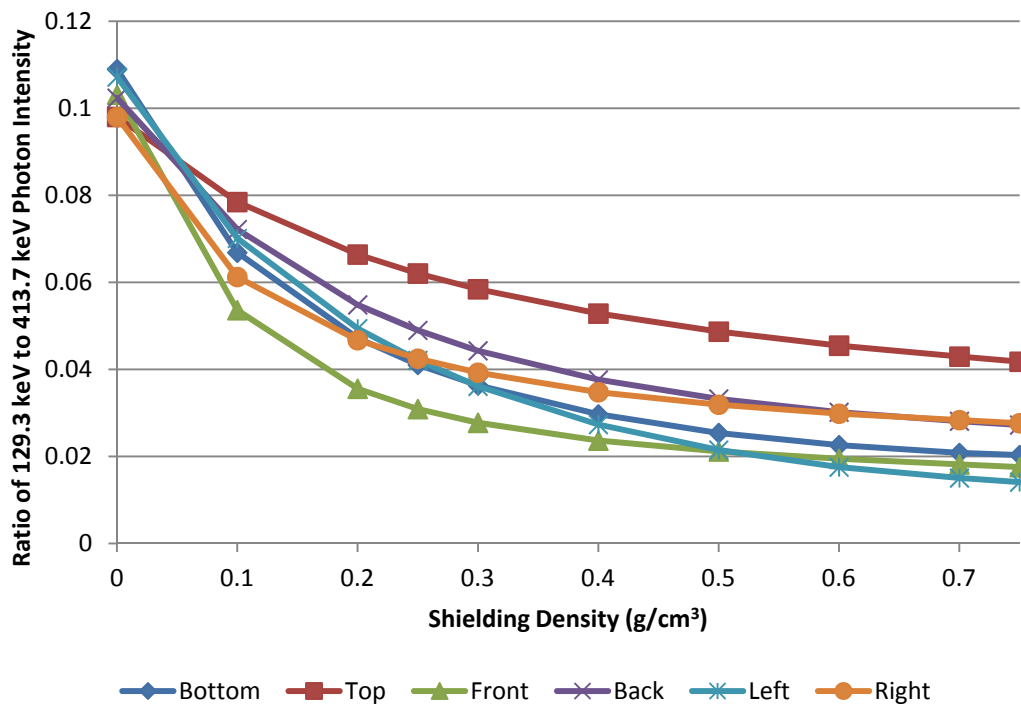
Figure-17: Results for SWB Model with Reduced Density Complex Sources

57

The results from the reduced density complex source model are presented in Figure-17. The maximum error identified for any of these points was 0.70%. The data showed a trend for the reduction in the 129.3 to 413.7 keV photon intensity ratio as the inter-source shielding density increased.

4.6.3 Discussion: Complex Source – Reduced Density

The behavior observed in the reduced density complex source is more consistent with the expected response for discrete sources spread through a shielding medium. Namely, as the amount of shielding between the source and the detector increases, the number of 129.3 keV photons relative to the number of 413.7 keV photons decreases, consistent with Section 3.3. This is opposite the trend identified in the complex source (Figure-14) and monoenergetic complex source (Figure-15) cases.

It is noted, however, that the observed behavior is not entirely consistent with the shielding equations. The intensity for photons through a given shielding medium should fall off logarithmically. As shown in Figure-18, the fall off for 129.3 keV photons is not a straight line when plotted logarithmically, and appears to be leveling off as density increases.

This finding is consistent with the observations in Section 4.5.3, namely, that as the amount of shielding increases, the fraction of photons born at higher energies and being detected in the energy band from 129-130 keV also increases, thereby obscuring the number of unattenuated gammas born at 129.3 keV.

58

It was considered that the observed behavior could have resulted, at least in part, by the overlapping intensity attenuations from the three sources, each with its own attenuation curves.
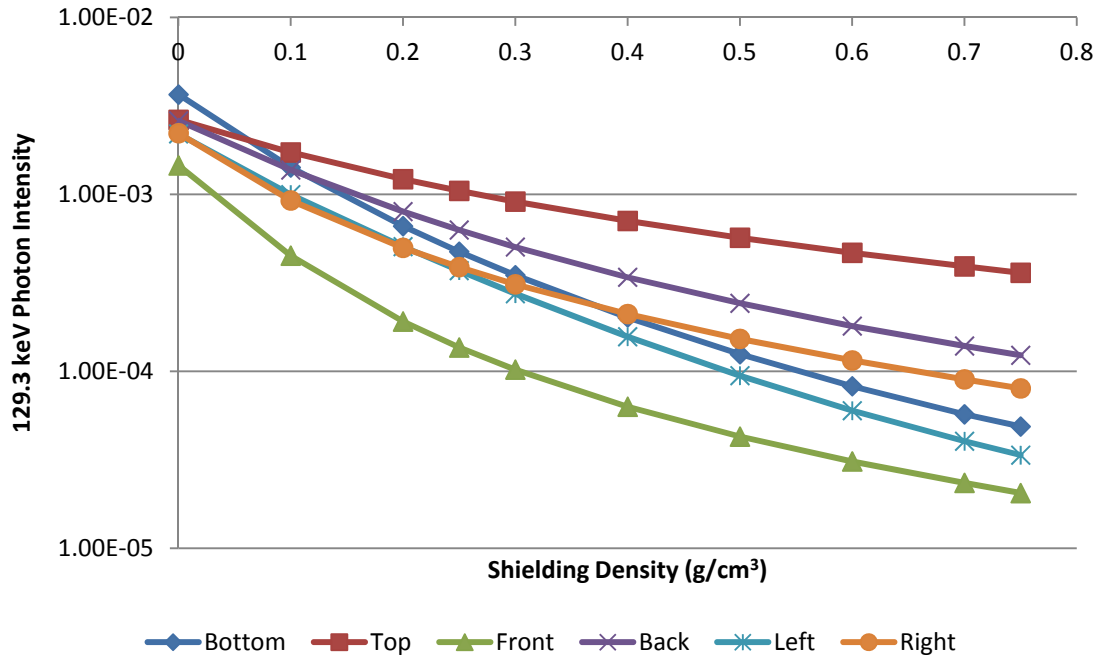
Figure-18: 129.3 keV Photon Intensity for Reduced Density Complex Source

In order to verify that the observed behavior was a primarily a result of buildup of low energy photons resulting from energy reducing interactions, such as photo electric effect and Compton scattering of high energy photons, the reduced density complex source model (see Section 4.6.1) was rerun with monoenergetic sources with the results being compared to the polyenergetic source model discussed above. The maximum error for any of the values considered in this comparison was 0.69% for the monoenergetic values and 0.19% for the polyenergetic values. The results are presented in Table-18.

59

**Table-18: Percentage of Low Energy Photons Born at 413.7 keV –
Reduced Density Source**

Detector Location	Inter-Source Shielding Density (g/cm^3)						
	0.1	0.2	0.3	0.4	0.5	0.6	0.7
Bottom	6.37%	11.01%	15.00%	19.91%	25.12%	30.17%	34.74%
Top	1.82%	2.35%	2.70%	3.03%	3.32%	3.56%	3.75%
Front	3.29%	5.77%	7.66%	9.57%	11.29%	12.87%	14.31%
Back	2.25%	3.32%	4.21%	5.12%	5.93%	6.66%	7.21%
Left	2.61%	4.26%	6.05%	8.56%	11.58%	15.08%	18.63%
Right	3.18%	4.75%	5.80%	6.80%	7.65%	8.30%	8.82%
	Percentage of 129-130 keV Photons born at 413.7 keV						

The percentage of photons being born at higher energies is greatly reduced as compared to those seen in the high density sources (see Table-17). However, they still account for a significant fraction of the low energy photons. Additionally, it is noted, that the contribution varies greatly dependent on the source geometry with respect to detector location. For example, at maximum density with the detector located at the top of the container, only 3.75% of the 129-130 keV photons were born at 413.7 keV, as compared to the detector being at the bottom, which resulted in 34.74% being born at 413.7 keV.

The variation of readings based on detector location indicates that a single photon spectrum reading taken at an arbitrary location may not provide useful information regarding the internal contents of the container, particularly as the density of materials within the container increases.

To fully understand the contribution of higher energy photons to the 129-130 keV bin, additional models were run for all the Pu-239 decay energies. The resulting percentages of 129-130 keV photons that were born at higher energies are shown in Table-19. The maximum error for any of the values considered in this comparison was 1.11% for the monoenergetic values and 0.19% for the polyenergetic values.

Table-19: Percentage of 129-130 keV Photons Born at Higher Energies – Reduced Density Source

Detector Location	Inter-Source Shielding Density (g/cm³)						
	0.1	0.2	0.3	0.4	0.5	0.6	0.7
Bottom	17.31%	28.44%	39.58%	52.28%	65.36%	78.15%	89.78%
Top	5.84%	7.36%	8.45%	9.37%	10.14%	10.81%	11.35%
Front	9.98%	16.77%	22.74%	28.43%	33.43%	38.22%	42.57%
Back	6.95%	9.96%	12.66%	15.28%	17.55%	19.59%	21.11%
Left	7.86%	12.41%	17.90%	25.14%	34.00%	44.28%	54.73%
Right	9.64%	13.97%	17.26%	20.04%	22.25%	24.07%	25.44%
Percentage of 129-130 keV Photons born at Higher Energies							

This information is also displayed graphically in Figure-19. As the density of the shielding matrix increases, the amount of buildup at the lower energies increases greatly, making the accurate determination of the intensity of unattenuated 129.3 keV gammas difficult.
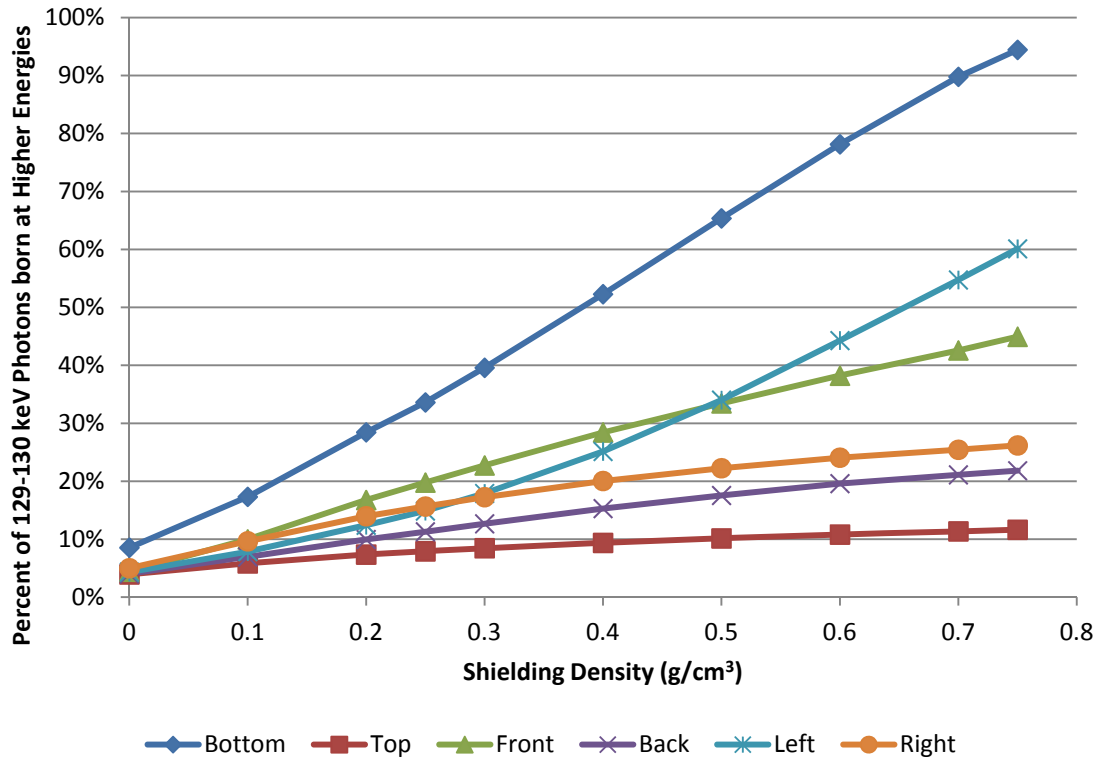
Figure-19: Percentage of 129-130 keV Energy Photons Born at Higher Energies – Reduced Density Source

While there are other Pu-239 decay gamma that could be used for the determination of a shielding ratio, they also have problems.

The 203.55 keV gamma is much lower in intensity than the 129.3 keV gamma (see Table-3), is harder to detect due to lower detector efficiency (Figure-3), and still susceptible to buildup from attenuation of higher energy photons (Table-20 and Figure-20). This conclusion is consistent with the ISOCS data (See Table-4), which often showed that the 203.55 keV gamma peak was indistinguishable from background.

62

**Table-20: Percentage of 203-204 keV Photons Born at Higher Energies –
Reduced Density Source**

Detector Location	Inter-Source Shielding Density (g/cm^3)						
	0.1	0.2	0.3	0.4	0.5	0.6	0.7
Bottom	17.89%	24.27%	28.80%	33.93%	38.89%	43.41%	48.08%
Top	11.32%	13.55%	14.77%	15.90%	16.76%	17.45%	18.05%
Front	16.09%	22.45%	26.41%	30.02%	33.03%	35.45%	37.90%
Back	11.85%	15.15%	17.31%	19.58%	21.51%	23.12%	24.45%
Left	13.50%	17.76%	21.07%	25.03%	29.18%	33.46%	37.62%
Right	13.83%	17.89%	20.30%	22.53%	24.31%	25.80%	26.88%
	Percentage of 203-204 keV Photons born at Higher Energies						
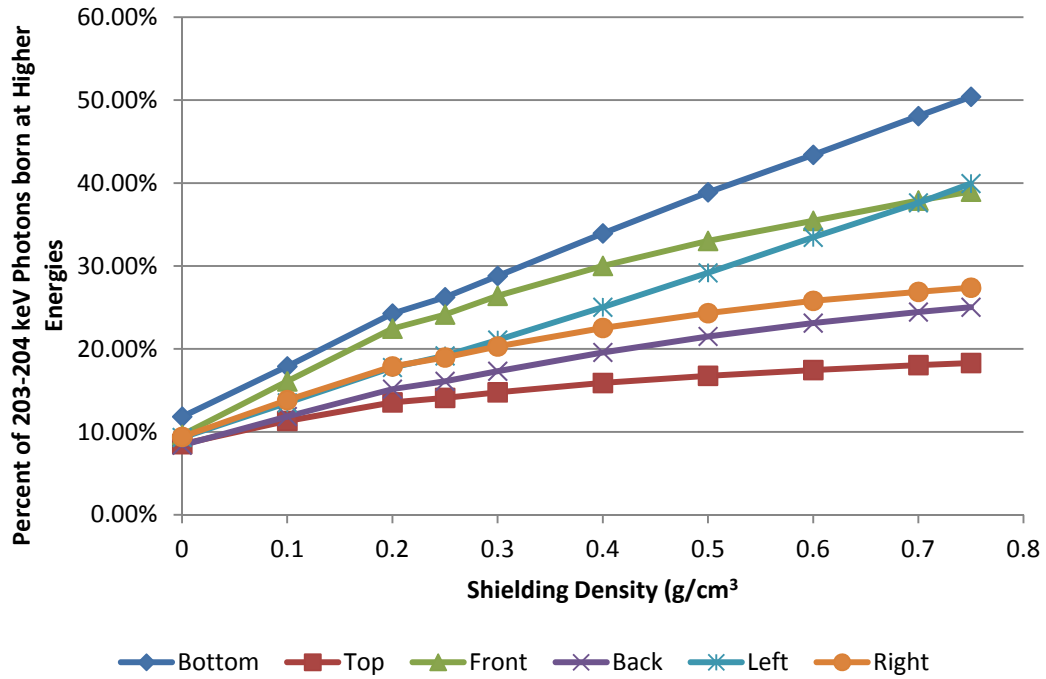
Figure-20: Percentage of Low Energy Photons Born at Higher Energies –

Reduced Density Source

63

As a result, the 203.55 keV peak is also not well suited for determining the shielding thicknesses. The maximum error for any of the values considered in Table-20 or Figure-20 was 0.55% for the monoenergetic values and 0.58% for the polyenergetic values.

The 375.05 keV peak, while relatively intense, is also not well suited for differential comparisons as it is very close in energy to the 413.7 keV peak, resulting in only minor differences in attenuation for a given shielding thickness. These variations are often within the statistical error margins of the measurements of the ISOCS, as demonstrated in Figure-4.

As a result of all these issues, it must be concluded that, while ISOCS can detect the presence of radioactive isotopes, the physical limitations that arise from the nature of the measurement system and the physical configuration of the SWBs and the contained waste limit the amount of precision these readings can have, and therefore the fundamental accuracy.

Chapter 5 Integrated Discussion

5.1   Summary of Objective and Methods

As established in Chapter 3, the specific objectives of this research were to determine if:

- Using the data available, the discrepancies between the SuperHENC and ISOCS assays can be explained

- ISOCS generates useful data when used for assay of SWBs

- The use of ISOCS can be improved to allow for better measurements in the future

To satisfy the research objectives, the assay data from ISOCS and SuperHENC were compared. Additionally, the ISOCS process was modeled in MCNPX. The modeling in MCNPX was performed iteratively to discover the behavior of distributed sources in a shielding matrix when measured with gamma spectroscopy.

5.2   Significant Observations

Two major trends were noted during the performance of the MCNPX models.

First, the presence of a distributed source in a distributed shielding material, such as surface contamination on large metal objects, results in energy specific photon attenuation that is inconsistent with a point source that is present behind a discrete shield. This results in the ratio of low energy to higher energy photons to converge on a seemingly fixed ratio at higher shielding densities.

65

Second, the allowed densities of shielding materials within the SWBs can result in significant buildup of low energy photons from the attenuation of higher energy photons.

The combination of the effects of a distributed source and buildup of low energy photons from attenuation of high energy photons results in conditions at the detector that may vary greatly for a given container based on the position of the detector.

Since the intensity of unattenuated low energy gammas from the decay of Pu-239 (or other TRU isotopes) relative to unattenuated high energy gammas cannot be reliably determined, the amount of shielding present between a discreet source and the detector cannot be reliably determined. Furthermore, since the sources are not discreet, nor necessarily evenly distributed, the accurate determination of shielding material is subject to significant uncertainty.

Since the amount of shielding cannot be reliably determined, the use of the attenuated intensity in conjunction with the shielding thickness to determine the unattenuated source strength is subject to significant uncertainty.

For example, if the ratio between the low energy photons to high energy photons is elevated as a result of the distribution of the source material as well as the buildup of low energy photons, the shielding thickness will be underestimated. As a result, for a given detector reading, when the shielding thickness is removed to determine the amount of material present, the source will be presumed to be smaller than it actually is. This conclusion is consistent with the discrepancy seen between ISOCS and SuperHENC in Table-1 and Appendix D.

66

5.3   Other Issues that May Impact the Use of ISOCS

The physics issues identified above are by no means the only potential issues that may complicate the use of ISOCS (or other gamma spectroscopy based systems) for assay of SWBs in the field.

Although Pu-239 is the primary isotope present within the SWBs, it is not the only one present. The other isotopes each have their own gamma emission spectrums which will serve to elevate the background of low energy photons, making it difficult to differentiate the unattenuated 129.3 keV gammas from the decay of Pu-239 (or other isotopes) from those being born at different energies. As the amount of shielding within the SWB increases, the difficulty of isolating a single low energy peak from the general noise of attenuated photons will increase, thereby further complicating the task of accurately determining shielding thickness and ultimately source strength.

Heterogeneity of the waste will result in greater variety of readings. In the models considered, the complexity and variability of the results increased significantly in moving from a homogenous source to a more complex, yet still relatively simple, arrangement. In actual TRU waste, a variety of complicated shapes composed of different materials will be present.

Similarly, the variations in ISOCS and SWB relative placement may result in inaccuracies. For example, the detector could be placed slightly closer or further away from the SWB. Additionally, the capabilities of the detector itself were not considered in the modeling. Any real world detector will have significant limitations on the accuracy

67

of measurements including, but not limited to angular and energy sensitivities, attenuation within the detector itself, and finite resolution.

Another potential confusing factor is the presence of background radiation. In the MCNPX models, only the photons added as part of the modeling are present. The presence of background radiation could further complicate the accurate determination of low energy peaks. In addition to the typical sources of background radiation, there may also be small amounts from other TRU containers in the vicinity, as the ISOCS assay is not performed within a shielded enclosure.

Although all of these issues could impact the efficacy of the use of ISOCS (or other gamma spectroscopy based assay systems) for in-situ measurements, and could be evaluated at length, it is believed that the physics issues evaluated within this thesis are more significant, and ultimately limit the theoretical maximum accuracy that the ISOCS or other gamma spectroscopy system can attain.

Chapter 6 Conclusions

As a result of the findings discussed in this thesis, the following conclusions are reached:

Research Objective 1: Using the data available, can the discrepancies between the
SuperHENC and ISOCS assays be explained

Conclusion: Yes. The buildup of low energy photons resulting from attenuation of high
energy photons as well as the effect on relative photon attenuation resulting from a
distributed source present upon a distributed shielding material results in an inflated ratio
of low energy photons to higher energy photons. This inflated ratio results in an
underestimation of the shielding present, thereby resulting in an underestimation of the
actual source strength. The magnitude of this effect varies greatly based on the shielding
density and the extent of shielding distribution, and are therefore do not behave like a
simple systematic error offset. As a result, the accuracy of the system depends greatly on
the composition of the waste. These conclusions are consistent with the discrepancy seen
between ISOCS and SuperHENC in Table-1 and Appendix D.

Research Objective 2: Does ISOCS generate useful data when used for assay of SWBs

Conclusion: Yes, though with significant limitations. As shown in the available ISOCS
and SuperHENC data, the results from ISOCS can be used as rough approximations of
the materials present, and provide a general indication of the materials present. It should
be noted, however, that the measurements will generally reflect lower quantities of
materials being present than actually are. Therefore, the ISOCS readings should be used

69

with caution, especially if being used for regulatory compliance.

Research Objective 3: Can the use of ISOCS be improved to allow for better measurements in the future

Conclusion: Yes, though with significant limitations that may not be practical. It was observed that different measurement locations resulted in significantly different results. Therefore, if multiple measurements were taken at different locations, and the highest reading was used, or perhaps the median reading with an offset, the discrepancy with SuperHENC data may be reduced, this is a topic for additional research. However, this would require a much more significant time commitment for the performance of assays.

Similarly the size of the containers or the mass of the contents could be reduced to help reduce the amount of potential shielding materials. This too may not be practical. The size of containers is set by specific needs, and is not within the control of the facility. Additionally, the cost for disposal is on a container basis, distributing the content between multiple containers will rapidly increase these costs.

Chapter 7 Recommendations

As discussed in the previous sections, there appear to be physical issues that limit the potential accuracy of a gamma spectroscopy system for the assay of large objects when used in the discussed configuration. However, there are several lines of research that could be investigated to improve the overall accuracy. These include but are not limited to further investigation on multiple readings from different angles and determining if these can be reliably correlated to container contents. In particular, it would be worth researching if some angles were more reliable than others for accurate detection, such as taking the reading from the location of either the highest or lowest on-contact radiation readings.

Additionally, some of the methods identified for neutron based systems may be applied to gamma spectroscopy based systems. For example, counting the system before and after adding a gamma source of known strength and using this information as a calibration point may yield more reliable information on shielding thickness allowing for a more accurate determination of source strength.

Another potential area of interest would be to pursue the significance of the convergence point for the ratios between high and low energy photons discussed in Section 4.3.3, including the significance of the ratio between mean free path lengths at the point of convergence for two given photon energies, if any.

Chapter 8 References

1. *WIPP Land Withdrawal Act*, P.L. 102 – 579, as amended by P.L. 104 – 201 (1996).

2. Environmental Protection Agency (1999). *Cancer Risk Coefficients for Environmental Exposure to Radionuclides, Federal Guidance Report No. 13*. EPA 402-R-99-001. U.S. Environmental Protection Agency. Washington, DC.

3. Department of Energy, Carlsbad Field Office, (2011) *Transuranic Waste Acceptance Criteria for the Waste Isolation Pilot Plant*, DOE/WIPP-02-3122, Carlsbad, NM.

4. *Occupational Radiation Protection* (2011). 10 CFR 835.

5. Abdurrahman, N. M., Simpson, A. P., Barber, S., (2005) *WIPP Certification of a New SuperHENC at Hanford for Assay of Transuranic Waste in Standard Waste Boxes,* BIL Solutions Inc., Fluor Hanford.

6. Franco, J., Menlove, H., Rael, C., Stoner, N., Clapham, M., (2001) *SuperHENC: Final Performance and Certification Summary,* BNFL Instruments, Inc., Los Alamos National Laboratory, Rocky Flats Environmental Technology Site.

7. Department of Energy (2007) *Preparation of Safety Basis Documents for Transuranic (TRU) Waste Facilities*, DOE-STD-5506, Washington, D.C.

8. McElroy, R. D., Croft, S., Young, B. M., *Non Destructive Assay Box Counter*,

Canberra Industries, Meriden, CT.

9. Chapman, M. J., Franco, J., Simpson, A., Santo, J., Menlove, H. O., Durel, F. M., (2003) *Operational and Regulatory Performance of Waste Crate Assay Systems at RFETS,* LA-UR- 03-0774, Los Alamos National Laboratory.

10. Simpson, A. P., Barber, S., Abdurrahman, N. M., (2006) *Innovations in the Assay of Un-Segregated Multi-Isotopic Grade TRU Waste Boxes with SuperHENC and Fram Technology,* BIL Solutions Inc., Fluor Hanford.

11. Bronson, F. L., CHP, Umbaugh, L., Booth L. F., CHP, Groff, D. W., (1999) *Use of In-Situ Gamma Spectroscopy to Support Decontamination and Decommissioning Activities,* Canberra Industries.

12. Canberra Industries, *MCNP Detector Efficiency Report for Detector S/N 4512*, Canberra Industries, Meriden, CT.

13. Brookhaven National Laboratory. *National Nuclear Data Center, information extracted from the Chart of Nuclides database, http://www.nndc.bnl.gov/chart/.* Brookhaven National Laboratory. Upton, New York.

14. Lamarsh, J. R., Baratta, A. J., (2001). *Introduction to Nuclear Engineering, Third Edition*. Prentice Hall. Upper Saddle River, New Jersey.

15. Los Alamos National Laboratory (2008). *MCNP – A General Monte Carlo N-Particle Transport Code, Version 5, Volume II: User's Guide,* LA-CP-03-0245.

Los Alamos National Laboratory. Los Alamos, New Mexico.

16. Los Alamos National Laboratory (2008). *MCNP – A General Monte Carlo N-Particle Transport Code, Version 5, Volume I: Overview and Theory,* LA-UR-03-1997. Los Alamos National Laboratory. Los Alamos, New Mexico.

74

Appendix A.   Example ISOCS Data

WASTE EXAMINATION TECHNIQUE
COVER PAGE

Waste Generator Site: Nevada Test Site, NSTEC Environmental Management TRU Project

Waste Stream Category: S5000

Waste Stream Name: Heterogeneous Debris

Surface Dose Rate of Loaded Standard Waste Box: 0.1 mR/hr gamma, 0.02 mRem/hr Neutron

Surface Contamination Survey of Loaded Standard Waste Box: < 20 dpm/100cm^2 α, < 200 dpm/100 cm^2 β + γ

See NTS master submittal for filtered liner bag data (circle one):   (Yes)   No

Number of Pages in Data Report: 22

Comments
Container Number: NT060209R
Generated from Livermore waste stream – NTLLNL-S5119 as listed in CCP-AK-NTS-001, Rev. 9

Waste Examination Expert

Name	Signature	Time/Date
Sherry Purzka	SherryPurzka	0844/11.03.08

WEF SUPV

Name	Signature	Time/Date
KEN BERTRAND	Ken Bert	0900/11-03-08

75

Appendix A. Example ISOCS Data (continued)

WASTE EXAMINATION TECHNIQUE
COVER PAGE

Waste Generator Site: Nevada Test Site, NSTEC Environmental Management TRU Project

Waste Stream Category: S5000

Waste Stream Name: Heterogeneous Debris

Surface Dose Rate of Loaded Standard Waste Box: 0.1 mR/hr gamma, 0.02 mRem/hr Neutron

Surface Contamination Survey of Loaded Standard Waste Box: < 20 dpm/100cm^2 α, < 200 dpm/100 cm^2 β + γ

See NTS master submittal for filtered liner bag data (circle one): (Yes)   No

Number of Pages in Data Report: 22

Comments
Container Number: NT060209R
Generated from Livermore waste stream – NTLLNL-S5119 as listed in CCP-AK-NTS-001, Rev. 9

Waste Examination Expert

Sherry Perzka	Slwjperzka	0844/11·03·08
Name	Signature	Time/Date

WEF SUPV

KEN BERTRAND	Ken Belt	0780/11·03·08
Name	Signature	Time/Date

Appendix A. Example ISOCS Data (continued)

NATIONAL SECURITY TECHNOLOGIES STANDARD OPERATING PROCEDURE

Title: Container Repackaging and Operations Procedure (SBI)	Page 38 of 38
Document No.: SOP-2151.564	Use Category: II
Revision No. 0	Periodic Review Due Date:08/25/10
Effective Date: 08/25/08	Quality Affecting: Yes

Appendix A
Area 5 Payload Container Evaluation Record
Page 1 of 1

PAYLOAD CONTAINER EVALUATION RECORD		Initials	Date
Container Identification Number: NT060209R		ЈТ	09/27/08
Container Type (circle One) SWB / Cargo Container / Drum / MacroPack		ЈТ	09/27/08
Nuclear Filter Vent(s) model 19DS serial number(s): KG-250 / KG-251			
Nuclear Filter Vents installed to manufactures specification: Sat ☒ Unsat ☐ Torque Wrench Number 009433 Calibration Due Date: 03/18/09		ЈТ	09/27/08
Bolts installed to manufactures specifications: 009429 Sat ☒ Unsat ☐ Torque Wrench Number Calibration Due Date: 03/18/09		SET	8/29/08 SET/29/
Container Inspection		**Initials**	**Date**
Evidence that the container is, or has been pressurized:	Yes ☐ No ☒	ЈТ	09/27/08
Potentially significant rust or corrosion, the load bearing capacity is suspect: (pitting, packing, flaking, or dark coloration on any outside surface).	Yes ☐ No ☒	ЈТ	09/27/08
Split seams, tears, obvious holes, pinholes, punctures (of any size), breaches, creases, broken welds, cracks or wall thinning:	Yes ☐ No ☒	ЈТ	09/27/08
Load bearing capacity suspect:	Yes ☐ No ☒	ЈТ	09/27/08
Fastener damaged such that the container will remain closed and is not in firm contact with the entire circumference of the container.	Yes ☐ No ☒	ЈТ	09/27/08
Dents, scraps, or scratches that make the container's structural integrity questionable or prevent the top and bottom surfaces from being parallel:	Yes ☐ No ☒	ЈТ	09/27/08
Comments: (If "Yes" or "Unsat" is marked on any item completely state the noncompliance and the corrective action taken.) N/A			

WH

Name: JON TANAKA	Signature: [signed]	KB8 09/29/08 Time/Date
WEF SUPV		
Name: KEN BERTRAND	Signature: [signed]	1700 9/29/08 Time/Date

GENERAL USE

77

Appendix A.   Example ISOCS Data (continued)

NATIONAL SECURITY TECHNOLOGIES STANDARD OPERATING PROCEDURE		
Title: **Waste Examination Technique (SBI)**	Page **15** of **18**	
Document No.: **SOP-2151.565**	Use Category:	**II**
Revision No. **0**	Periodic Review Due Date: **08/25/10**	
Effective Date: **08/25/08**	Quality Affecting: **Yes**	

Appendix A
Payload Container Coversheet
Page 1 of 1

	Initals	Date
Container Number: NT060209R		
Container Type (circle One): SWB / Cargo Container / Drum / Macropack		
Container Tare Weight (empty): 640.00 Pounds 290.91 Kg Scale ID# N/A		9/27/2008
Container Tare Weight (Assembled): 682.00 Pounds 310.00 Kg Scale ID# N/A		9/27/2008
Container Gross Weight: 1350.00 Pounds 613.64 Kg Scale ID# 27083456		9/29/2008
Packaging Configuration: Metal SWB, plastic bag liner, fiberboard liner (no lid)		9/27/2008
Closure Method: Twisted and taped		9/29/2008
Gasket(s) Present at Closure: Yes		9/29/2008
Tamper Indicating Device (TID) applied: 0041, 0042		9/29/2008
Layers of Confinement: 1		9/29/2008
Container Fill Factor: 90 %		9/29/2008

Source Container Number(s):

NT26S	N/A	N/A	N/A	N/A

Comments
Additonal scale used ID# 27083459. All operations performed in accordance with SOP-2151.565 Rev 0. A/V checks
performed on 9/27/08 on Media No. 092608-2. All bags and wraps breached or left unsealed.

Waste Examination Expert

Name: Shern Puzka   Signature: Shern Puzka   Time/Date: 1349/ 9-29-08

WEF SUPV

Name: KEN BERTRAND   Signature: Ken Bett   Time/Date: 1436/9-29-08

'GENERAL USE'

78

Appendix A.   Example ISOCS Data (continued)

NATIONAL SECURITY TECHNOLOGIES STANDARD OPERATING PROCEDURE

Title: **Waste Examination Technique (SBI)**	Page **15** of **18**	
Document No.: **SOP-2151.565**	**Use Category:**	**II**
Revision No. **0**	Periodic Review Due Date: **08/25/10**	
Effective Date: **08/25/08**	Quality Affecting: **Yes**	

Appendix A
Payload Container Coversheet
Page 1 of 1

		Initials	Date
Container Number: NT060209R			
Container Type (circle One): SWB / Cargo Container / Drum / MacroPack			
Container Tare Weight (empty): N/A pounds N/A Kg Scale ID# N/A			
Container Tare Weight (assembled): N/A pounds N/A Kg Scale ID# N/A			
Container Gross Weight: N/A pounds N/A Kg Scale ID# N/A			
Packaging Configuration: N/A			
Closure Method: N/A			
Gasket(s) present at Closure: N/A			
Tamper Indicating Device (TID) applied: 0523			
Layers of Confinement: N/A			
Container Fill Factor: N/A %			

Source Container Number(s):

N/A	N/A	N/A	N/A	N/A

Comments
TID #0042 replaced with 0523 as a result of headspace gas sampling and the TID being placed over the sample port.

Waste Examination Expert

Lois Gregory _____ (Signature) _____ 1046/11/19/08
Name   Signature   Time/Date

WEF SUPV

Ken Bernard _____ (Signature) _____ 0846/11/26/08
Name   Signature   Time/Date

GENERAL USE ✓

Appendix A. Example ISOCS Data (continued)

NATIONAL SECURITY TECHNOLOGIES STANDARD OPERATING PROCEDURE

Title: **Waste Examination Technique (SBI)**	Page **15** of **18**
Document No.: **SOP-2151.565**	Use Category: **II**
Revision No. **0**	Periodic Review Due Date: **08/25/10**
Effective Date: **08/25/08**	Quality Affecting: **Yes**

Appendix A
Payload Container Coversheet
Page 1 of 1

		Initials	Date
Container Number: NT060209R			
Container Type (circle One): SWB / Cargo Container / Drum / MacroPack			
Container Tare Weight (empty): N/A pounds N/A Kg Scale ID# N/A			
Container Tare Weight (assembled): N/A pounds N/A Kg Scale ID# N/A			
Container Gross Weight: N/A pounds N/A Kg Scale ID# N/A			
Packaging Configuration: N/A			
Closure Method: N/A			
Gasket(s) present at Closure: N/A			
Tamper Indicating Device (TID) applied: 0523			
Layers of Confinement: N/A			
Container Fill Factor: N/A %			

Source Container Number(s):

N/A	N/A	N/A	N/A	N/A

Comments
TID #0042 replaced with 0523 as a result of headspace gas sampling and the TID being placed over the sample port.

Waste Examination Expert

Lois Gregory		1046 / 11/19/08
Name	Signature	Time/Date

WEF SUPV

Ken Bernard		0846 / 11/26/08
Name	Signature	Time/Date

GENERAL USE

80

Appendix A. Example ISOCS Data (continued)

NATIONAL SECURITY TECHNOLOGIES STANDARD OPERATING PROCEDURE

Title: **Waste Examination Technique (SBI)**		Page **16** of **18**	
Document No.: **SOP-2151.565**		Use Category:	**II**
Revision No. **0**		Periodic Review Due Date: **08/25/10**	
Effective Date: **08/25/08**		Quality Affecting: **Yes**	

Appendix B
Payload Container Coversheet
Page 1 of 2

Gross Weight: 1350.0 lbs 613.6 kgs			Container Number: NT060209R		
WMP	**%**	**Estimated Weight**	**WMP**	**%**	**Estimated Weight**
Iron based metals/alloys	94.50%	1275.8 lbs 579.9 kgs	Plastics (waste materials)	1.00%	13.5 lbs 6.1 kgs
Aluminum-based metal/alloys	2.00%	27.0 lbs 12.3 kgs	Organic matrix	0.00%	0.0 lbs 0.0 kgs
Other metals	0.50%	6.8 lbs 3.1 kgs	Inorganic matrix	0.50%	6.8 lbs 3.1 kgs
Other inorganic materials	0.50%	6.8 lbs 3.1 kgs	Soils	0.00%	0.0 lbs 0.0 kgs
Cellulosics	0.50%	6.8 lbs 3.1 kgs	Steel (packaging materials)	0.00%	0.0 lbs 0.0 kgs
Rubber	0.50%	6.8 lbs 3.1 kgs	Plastics (packaging materials)	0.00%	0.0 lbs 0.0 kgs

Payload Container Contents:

9/27/08 Media No. 092708-1
WEE S. Peczka, WH J. Tanaka, IW J. Woods, IW T. Hicks, LB K. Kackman, RCT M. Cotton/RCT S. Pennock

SWB Bag plastic bag stub with rubber o-ring and plastic tape (NTS generated) (99% plastic, 1% rubber) iron based metal glovebox with iron based metal hardware, copper tubing, iron based metal ports, rubber glovebox gloves, Plexiglas panels, rubber gasket material, plastic bag out bag, (90% iron based metal, 8% plastic, 1% other metals, 1% rubber) containing plastic straps (100% plastic), Aquaset absorbent added to ensure no liquids from CC Wet application are present (NTS generated) (100% other inorganic), iron based metal tools (100% iron based metal), iron based metal filters (100% iron based metal), iron based scraper with plastic handle (70% iron based metal, 30% plastic), plastic j-knife with iron based metal blade (NTS generated) (99% plastic, 1% iron based metal), iron based metal flange (100% iron based metal), iron based metal scraper (100% iron based metal), cellulosics labels (100% cellulosics), iron based metal bolts (100% iron based metal) covered in plastic sheeting (100% plastic) with plastic tape (100% plastic), Iron based metal plate (100% iron based metal) from glovebox with plastic tape (100% plastic) Plastic bag out bag with plastic tape with rubber o-ring (99% plastic, 1% rubber) containing iron based metal HEPA unit with cellulosics filter media (98% iron based metal, 2% cellulosics), iron based metal clamp (100% iron based metal) and plastic clamp (100% plastic). Copper piping (100% other metals) with plastic tape (100% plastic). Wood framed HEPA filter with cellulosics filter media, rubber gaskets, iron based metal clamps, plastic bag,

GENERAL USE

Appendix A. Example ISOCS Data (continued)

NATIONAL SECURITY TECHNOLOGIES STANDARD OPERATING PROCEDURE		
Title: **Waste Examination Technique (SBI)**		Page 17 of 18
Document No.: **SOP-2151.565**	**Use Category:**	**II**
Revision No. **0**	Periodic Review Due Date: **08/25/10**	
Effective Date: **08/25/08**	Quality Affecting: **Yes**	

Appendix B
Payload Container Coversheet
Page 2 of 2

Payload Container Contents Continued: NT0660092R

cellulosics labels, copper tubing (95% cellulosics, 2% iron based metal, 1% other metals, 1% plastic, 1% rubber)
Iron based metal cylindrical HEPA unit with cellulosics filter media with cellulosics labels (98% iron based metal, 2% cellulosics) contained in plastic bag (100% plastic) with plastic tape (100% plastic). Plastic bag out bag with plastic tape with rubber o-ring (99% plastic, 1% rubber) containing wood framed HEPA unit
with rubber tubing, plastic tape, and cellulosics filter media (96% cellulosics, 3% rubber, 1% plastic)
Plastic bag out bag with rubber o-ring (99% plastic, 1% rubber) with plastic tape (100% plastic) containing iron based metal HEPA with cellulosics filter media, rubber tubing on end with iron based metal clamps (97% iron based metal, 2% rubber, 1% cellulosics) Plastic bag with plastic tape (100% plastic) containing brass fitting (100% other metals)
Aluminum based metal scrap piece (100% aluminum based metals). Aluminum based metal scrap piece with rubber gasket attached (99% aluminum based metals, 1% rubber).Iron based metal framing (100% iron based metal) with rubber gaskets (100% rubber) attached. Plastic bag out bag with plastic tape (100% plastic), iron based metal screws (100% iron based metal), rust (100% iron based metal), rubber band (100% rubber). Rubber glove (100% rubber)
Tac cloth (NTS generated) (99% cellulosics, 1% inorganic materials), plastic tape (100% plastic), rubber o-ring (100% rubber), rubber glove (NTS generated) (100% rubber), plastic bag (NTS generated) (100% plastic) with iron based metal wire (NTS generated) (100% iron based metal), iron based metal scrap (100% iron based metal), iron based metal bolts (100% iron based metal), iron based metal tool (100% iron based metal), cellulosics & plastic label (50% plastic, 50% cellulosics), absorbent (100% inorganics). Tac cloth (NTS generated) (99% cellulosics, 1% inorganic materials)Tac cloth (NTS generated) (99% cellulosics, 1% inorganic materials) with metal shavings (100% iron based metal)Tac cloth (NTS generated) (99% cellulosics, 1% inorganic materials) with iron based metal nuts & bolts (100% iron based metal), cellulosics debris(100% cellulosics) & metal shavings (100% iron based metal)
Wood framed HEPA filter with plastic bag & plastic tape, cellulosics labels, iron based flange with iron based metal port covers, metal and cellulosics filter media (60% cellulosics, 39% iron based metal, 1% plastic). Tac cloth (NTS generated) (99% cellulosics, 1% inorganic materials) iron based metal clamp (100% iron based metal), iron based metal nuts (100% iron based metal), bolts, & washers (100% iron based metal), plastic tape (100% plastic), plastic sheeting (100% plastic) Plastic bag (NTS generated) with plastic tape (NTS generated)*(100% plastic), & absorbent (100% inorganics)
09/29/08, Media No. 092708-1WEE D. DeGering, WH L. Kinstad, IW M. McClelland, IW D. Kranjcevich, LB C. Kackman
Plastic bag with plastic tape (100% plastic) with copper pipe (100% other metals) and metal valve assembly (100% iron based metal), plastic sheeting (NTS generated) (100% plastic) with iron based hardware and shavings (100% iron based metal).

Waste Handler

Jon Tonka _____ _____ 1147 / 10/02/08
Name   Signature   Time/Date

Waste Examination Expert

Sherry Puzka _____ Sherry Puzka _____ 1235 / 10/02/08
Name   Signature   Time/Date

GENERAL USE

Appendix A. Example ISOCS Data (continued)

NATIONAL SECURITY TECHNOLOGIES ORGANIZATION PROCEDURE

Document Number: OP-2151.522	Effective Date: 09/18/08
Revision Number: 14	Page 17 of 19

APPENDIX H
Container Radioisotope Inventory Control Form
Page 1 of 1

Payload Container ID NT060209R

Date	Time	Parent Container / Group #	Container PE-g		Container FGE	
			In	Total	In	Total
9/27/08	1425	NT26S / Group Three	28.3	28.3	18.54	18.54

N A

WEF SUPV			
KEN BERTRAD	Ren Bert	9-29-98/1434	
Name	Signature	Date / Time	
NFM			
Sheryl Pfeiffer		10/1/08 1855	
Name	Signature	Date / Time	

† = TSR/DSA Control

83

Appendix A. Example ISOCS Data (continued)

NATIONAL SECURITY TECHNOLOGIES ORGANIZATION PROCEDURE

Document Number: OP-2151.522	Effective Date: 11/10/08
Revision Number: 15	Page 18 of 19

APPENDIX I
Authorization to Reassign MAR Value
Page 1 of 1

Waste Container Number: NT060209R		Date: 11/18/08
Methodology Used for Change: ISOCS	Data Package Number: SWB 060209R SP 11/20/00 NT060209R	

Description of Change (provide brief summary of changes and attach data package):

Update of actual isotopic values for SWB NT060209R. The current assigned PE-g and FGE is based off of the full value of the parent OSB containers that were loaded into NT060209R. This ISOCS measurement is an accurate representation of the package activity and not an estimate.

Proposed New Values:
Pe-G – 27.10
Pe-G + 1ó – 27.30
FGE – 14.60
FGE + 1ó – 14.80
4820nCi/gm

Justification (include references to technical documents originating or justifying this change, as applicable):
ISOCS measurement of payload container NT060209R after repackaging. ISOCS data package SWB_NT060209R attached.

NFM

Name	Signature	11/20/08 0900 Date / Time

Appendix A.   Example ISOCS Data (continued)

Radioassay Data Sheet
Cabrera Services, Inc.

Header Information

Container ID:	SWB NT060209R
Assay Method:	ISOCS Assay
Assay Software:	Genie 2000 V3.1; Geometry Composer V4.2
Procedure and Revision:	OI-2151.318 Revision 0
Assay Date/Time:	9/29/08 11:07 AM
Container Net Weight:	322 kg
QC Replicate (Yes/No):	No Results: N/A

Calculated Totals

Waste Classification (TRU or LLW):	TRU			
TRU Activity Concentration:	4.82E+03	±	9.64E+01	nCi/gram
Plutonium Equivalent Mass (PE-g):	2.71E+01	±	5.06E-01	gram
Plutonium Equivalent Activity (PE-Ci):	1.67E+00	±	N/A	PE-Ci
Fissile Gram Equivalent (FGE):	1.46E+01	±	3.87E-01	gram
Total Decay Heat (W):	4.94E-02	±	9.90E-04	W
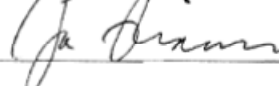
Applied Isotopic Mass Distributions

Pu-238	0.02%		Pu-241	0.40%
Pu-239	93.27%		Pu-242	0.05%
Pu-240	6.26%			
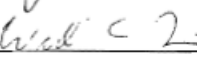
Summary of Assay Results

Nuclide	Activity Ci			Concentration nCi/gram		
Pu-238	5.45E-02	±	1.46E-03	1.69E+02	±	4.53E+00
Pu-239	9.09E-01	±	2.43E-02	2.82E+03	±	7.55E+01
Pu-240	2.27E-01	±	6.08E-03	7.05E+02	±	1.89E+01
Pu-241	6.46E+00	±	1.73E-01	2.01E+04	±	5.37E+02
Pu-242	3.09E-05	±	8.28E-07	9.59E-02	±	2.57E-03
Am-241	3.61E-02	±	1.83E-02	1.12E+03	±	5.66E+01
Np-237	3.90E-04	±	3.12E-05	1.21E+00	±	9.69E-02
Am-243	4.09E-04	±	3.86E-05	1.27E+00	±	1.20E-01
Cm-243	1.97E-04	±	1.39E-05	6.12E-01	±	4.31E-02

	Calculated	+ 1 Sigma	+2 Sigma
PE-g	2.71E+01	2.73E+01	2.76E+01
FGE	1.46E+01	1.48E+01	1.50E+01

Comments

All errors quoted at 1-sigma unless otherwise stated
FGE represents Pu-239 fissile gram equivalent

Signatures

Operator: _____   Date: 11/14/08

SME: _____   Date: 11/14/2008

WGS: _____   Date: 11-12-08

OSB Project Pu-Ratio, PE-FGE Determination

	A	B	C	D	E	F	G	H	I	J	K	L	M	N	O
1	Weight (g)	322340	Pu-239 (nCi/g)	2.82E+03		Description	SW8 NT060209R								
2															
3	Radionuclide	Act Conc (nCi/g)	Activity (Ci)	Activity (Bq)	PE-g/Bq	PE-g	PE-g Error at 1-sig	PE-Ci	Decay Heat (W)	Decay Heat Error at 1-sig	Sp. Activity (Ci/g)	Mass (g)	Pu-239 FGE	FGE
4	Pu-238	1.692E+02	5.454E-02	2.018E+09	3.90E-10	7.870E-01	2.107E-02	4.958E-02	1.806E-03	4.837E-05	1.730E-01	3.153E-03	3.562E-04	9.xxx
5	Pu-239	2.820E+03	9.090E-01	3.363E+10	4.35E-10	1.463E+01	3.918E-01	9.090E-01	2.818E-02	7.546E-04	6.290E-02	1.445E+01	1.445E+01	3.8xx
6	Pu-240	7.050E+02	2.272E-01	8.408E+09	4.35E-10	3.658E+00	9.794E-02	2.272E-01	7.074E-03	1.894E-04	2.300E-01	9.880E-01	2.223E-02	5.9xx
7	Pu-241	2.005E+04	6.463E+00	2.391E+11	8.50E-12	2.033E+00	5.443E-02	1.267E-01	2.057E-04	5.508E-06	1.040E-02	6.214E-02	1.398E-01	3.7xx
8	Pu-242	9.588E-02	3.091E-05	1.144E+06	4.09E-10	4.677E-04	1.252E-05	2.810E-05	9.108E-07	2.439E-08	3.970E-03	7.785E-03	5.839E-05	1.5xx
9	Am-241	1.120E+03	3.610E-01	1.336E+10	4.44E-10	5.931E+00	2.999E-01	3.610E-01	1.207E-02	6.103E-04	3.470E+00	1.040E-01	1.946E-03	9.xxx
10	Np-237	1.210E+00	3.900E-04	1.443E+07	4.60E-10	6.638E-03	5.318E-04	3.900E-04	1.143E-05	9.159E-07	7.130E-04	5.470E-01	8.205E-03	6.5xx
11	Am-243	1.270E+00	4.094E-04	1.515E+07	4.44E-10	6.725E-03	6.349E-04	4.094E-04	1.315E-05	1.242E-06	2.020E-01	2.027E-03	2.614E-05	2.4xx
12	Cm-243	6.120E-01	1.973E-04	7.299E+06	2.61E-10	1.905E-03	1.342E-04	1.409E-04	7.180E-06	5.058E-07	5.220E+01	3.779E-06	1.890E-05	1.2?
13	Cm-244	0.000E+00	0.000E+00	0.000E+00	2.11E-10	0.000E+00	0.000E+00	0.000E+00	0.000E+00	0.000E+00	8.180E+01	0.000E+00	0.000E+00	0.000x
14	Cm-245	0.000E+00	0.000E+00	0.000E+00	4.60E-10	0.000E+00	0.000E+00	0.000E+00	0.000E+00	0.000E+00	1.740E-01	0.000E+00	0.000E+00	0.00x
15	Cf-249	0.000E+00	0.000E+00	0.000E+00	4.91E-10	0.000E+00	0.000E+00	0.000E+00	0.000E+00	0.000E+00	4.140E+00	0.000E+00	0.000E+00	0.00x
16	U-233	0.000E+00	0.000E+00	0.000E+00	1.15E-10	0.000E+00	0.000E+00	0.000E+00	0.000E+00	0.000E+00	9.760E-03	0.000E+00	0.000E+00	0.00x
17	Total	2.487E+04	8.016E+00	2.966E+11		2.705E+01	5.064E-01	1.675E+00	4.937E-02	9.900E-04		1.617E+01	1.462E+01	3.870E-01
18	TRU	4.817E+03												

86

Appendix A.   Example ISOCS Data (continued)

```
Date:           Monday, September ...
Description:    SWB_NT060209R
Comment:        SWB_NT060209R
File Name:      c:\genie2k\isocs\data\geometry\in-situ\simple_box\swb060209r.geo
Software:       ISOCS
Template:       SIMPLE_BOX, Version: default
Detector:       6185
Environment:    Temperature= 22 C, Pressure= 760 mmHg, Rel.Humidity=  30%
Integration:    Convergence= 1.00%, MDRPN= 2^(4) CRPN= 2^(4)

                                Dimensions (inch):
# Geometry Compon.      d1      d2      d3      d4      d5      d6   Material  D(g/cm3) R.Conc.

1  Box                 (0.16)  71.00   36.00   54.50                 csteel    7.86
2  Source-Top Layer     32.00  Box wall thickness reduced           ss50cl50  0.16    1.00
3  Source-Bot Layer            from 0.2 to 0.16 (balance            none
4  Absorber1                   nuclide activities as a              none
5  Absorber2                   function of energy).                 none
6  Source-Detector      60.00                      9/29/2008        none

Collimator:     50mm-180d_old
                oldISOCS_50mm_side_180deg_collimation_[no_collimator]
List_of_energies for efficiency curve generation:

 45.0   59.5  100.0  150.0  200.0  300.0  500.0  600.0  700.0  1000.0
1400.0 1700.0 2000.0
```

87
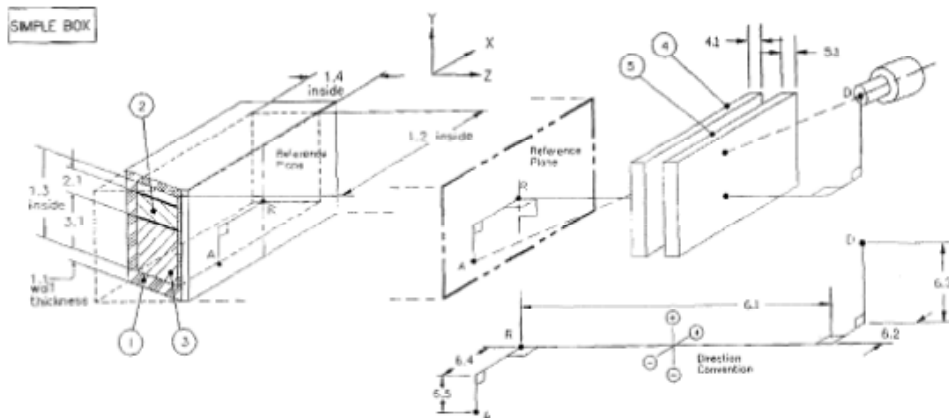
Appendix A.   Example ISOCS Data (continued)

```
Filename: C:\GENIE2K\CAMFILES\NTS TRU Repack\SWBNTO60209R.CNF

Report Generated On              : 9/29/2008  12:06:28 PM

Sample Title                     : SWB NT060209R
Sample Description               : Box Weight 1350 lbs.
Sample Identification            : SWB NT060209R
Sample Type                      : 6185
Sample Geometry                  :

Peak Locate Threshold            :   3.00
Peak Locate Range (in channels)  :   100 -  8192
Peak Area Range (in channels)    :   100 -  8192
Identification Energy Tolerance  :   1.500 FWHM

Sample Size                      : 3.223E+005 gram

Sample Taken On                  :
Acquisition Started              : 9/29/2008  11:07:43 AM

Live Time                        :    1800.0 seconds
Real Time                        :    1821.1 seconds

    d Time                       :    1.16 %


            Energy Calibration Used Done On       : 9/23/2008
            Efficiency Calibration Used Done On   : 9/29/2008
            Efficiency ID                         : SWB_NT060209R
```

88

```
C**..............  P E A K   A N A L Y S I S   R E P O R T  ............  **?**
C*****************************************************************************

    Detector Name:   6185DIG
    Sample Title:    SWB NT060209R
    Peak Analysis Performed on:  9/29/2008  12:06:28 PM
              Peak Analysis From Channel:    100
              Peak Analysis To Channel:     8192

    Peak  ROI   ROI     Peak    Energy   FWHM  Net Peak   Net Area   Continuum
    No. start  end   centroid   (keV)   (keV)    Area     Uncert.     Counts

      2   127-  140    135.79    49.52   2.18  9.83E+003   816.89    3.61E+004
      3   155-  171    163.26    59.58   1.68  7.33E+005  2108.91    8.44E+004
      4   190-  213    205.63    75.09   1.85  1.33E+004   880.82    2.70E+004
  M   5   224-  290    233.50    85.30   2.31  5.14E+003   296.55    2.42E+004
  m   6   224-  290    259.11    94.68   2.32  1.41E+004   342.50    2.38E+004
  m   7   224-  290    270.19    98.74   2.33  3.93E+004   470.68    2.25E+004
  m   8   224-  290    282.05   103.08   2.34  2.32E+004   393.04    1.99E+004
  M   9   295-  323    304.02   111.13   2.30  7.44E+003   298.89    2.00E+004
  m  10   295-  323    314.82   115.08   2.31  6.67E+003   289.54    1.94E+004
  M  11   334-  362    342.76   125.31   1.71  5.76E+003   233.70    1.23E+004
  m  12   334-  362    353.78   129.35   1.72  2.22E+004   346.94    9.86E+003
     13   385-  415    393.91   144.05   1.90  3.66E+003   740.35    1.59E+004
  C  14   432-  476    440.92   161.26   2.71  1.27E+003   198.44    9.49E+003
  m  15   432-  476    467.12   170.86   2.72  7.53E+002   176.88    9.44E+003
  M  16   514-  577    534.76   195.63   1.70  4.01E+002   122.76    5.39E+003
  m  17   514-  577    556.56   203.62   1.71  2.56E+003   149.66    4.74E+003
  m  18   514-  577    568.62   208.03   1.71  5.79E+003   195.85    4.17E+003
     19   646-  659    652.91   238.90   2.15  3.93E+002   229.85    2.95E+003
     20   691-  704    698.09   255.45   1.68  4.29E+002   204.65    2.31E+003
  M  21   803-  825    812.14   297.22   1.43  1.96E+002    75.43    1.58E+003
  m  22   803-  825    820.13   300.14   1.43  1.31E+002    70.20    1.54E+003
     23   847-  859    852.17   311.88   1.53  6.75E+002   167.47    1.55E+003
     24   873-  890    882.78   323.09   2.18  7.05E+002   204.40    1.84E+003
  M  25   901-  927    909.31   332.80   1.75  2.47E+003   122.69    1.58E+003
  m  26   901-  927    917.16   335.68   1.75  1.04E+003    92.36    1.71E+003
  M  27   937-  967    942.81   345.07   1.54  2.06E+003   114.60    1.36E+003
  m  28   937-  967    961.44   351.90   1.55  2.78E+002    62.06    1.01E+003
  M  29   996- 1054   1006.26   368.31   1.92  9.27E+002    82.93    1.19E+003
  m  30   996- 1054   1024.82   375.11   1.93  6.57E+003   171.08    1.02E+003
  m  31   996- 1054   1039.26   380.40   1.93  1.38E+003    87.63    8.48E+002
     32  1065- 1083   1073.46   392.92   1.86  2.13E+003   167.92    9.13E+002
  M  33  1123- 1172   1130.33   413.75   1.76  5.71E+003   156.33    6.05E+002
  m  34  1123- 1172   1154.37   422.55   1.77  3.89E+002    54.52    4.90E+002
  m  35  1123- 1172   1165.72   426.71   1.77  8.19E+001    40.61    4.73E+002
     36  1224- 1241   1233.31   451.46   2.06  6.92E+002   104.56    3.92E+002
     37  1387- 1406   1395.84   510.99   2.10  5.22E+002    80.54    2.69E+002
  C  38  1585- 1603   1593.10   583.23   1.63  2.48E+002    68.07    2.30E+002
     39  1657- 1674   1664.23   609.28   1.93  3.14E+002    69.79    2.34E+002
     40  1686- 1697   1690.88   619.04   0.78  7.40E+001    41.37    1.23E+002
     41  1802- 1820   1809.36   662.43   1.93  3.45E+002    72.53    2.44E+002
  M  42  1966- 1993   1972.26   722.09   1.75  1.71E+002    34.93    1.47E+002
```

89

Appendix A.   Example ISOCS Data (continued)

	Peak No.	ROI start	ROI end	Peak centroid	Energy (keV)	FWHM (keV)	net peak Area	net Area Uncert.	ct/cnnt Counts
m	43	1966-	1993	1987.83	727.79	1.76	3.60E+001	22.84	1.38E+002
	44	2481-	2497	2488.99	911.33	1.58	1.50E+002	45.56	1.01E+002
	45	2546-	2558	2551.80	934.34	0.58	4.46E+001	29.03	5.44E+001
	46	2641-	2653	2646.40	968.98	0.67	6.38E+001	38.18	9.92E+001
	47	3053-	3068	3060.23	1120.54	1.91	7.45E+001	40.13	9.35E+001
	48	3980-	4003	3990.67	1461.30	1.92	9.49E+002	65.81	3.56E+001
	49	4811-	4829	4820.49	1765.21	2.66	1.02E+002	23.29	9.50E+000
	50	7135-	7156	7145.31	2616.63	1.79	2.24E+002	31.82	1.06E+001

M = First peak in a multiplet region
m = Other peak in a multiplet region
F = Fitted singlet

Errors quoted at 1.960 sigma

90

Appendix A.   Example ISOCS Data (continued)

```
C   NUCLIDE IDENTIFICATION REPORT ····
C ···································································

    Sample Title:        SWB NT060209R
    Nuclide Library Used: C:\GENIE2K\CAMFILES\NTS_OSB_TRU_Expanded

    ···················   IDENTIFIED NUCLIDES   ···················
```

Nuclide Name	Id Confidence	Energy (keV)	Yield (%)	Activity (nCi/gram)	Activity Uncertainty
BI-211	0.475	351.10*	12.20	1.53179E-002	3.62113E-003
		404.80	4.10		
		426.90*	1.90	3.11451E-002	1.55793E-002
		831.80	3.30		
NP-236B	0.926	94.67*	23.40	1.04256E+000	1.91265E-001
		98.44*	38.00	1.54218E+000	2.74095E-001
		99.55	0.23		
		104.20*	7.20	4.21828E+000	7.34855E-001
		111.00*	17.70	4.52067E-001	7.45594E-002
		158.35	3.96		
		160.33*	31.50	2.63289E-002	5.01119E-003
NP-237	0.396	57.10	0.39		
		86.48*	12.40	1.11100E+000	2.26022E-001
		87.99	0.14		
		92.29	1.68		
		94.64*	0.60	4.06598E+001	2.75582E+001
		95.87	2.73		
		108.00	1.27		
		117.70	0.16		
		143.25*	0.43	6.06801E+000	1.50524E+000
		151.41	0.23		
		194.95*	0.18	1.32610E+000	4.49206E-001
		212.29	0.16		
Np-237B	0.890	29.37	15.00		
		86.48*	7.40	1.86168E+000	4.10477E-001
		94.65*	5.62	4.34091E+000	8.63175E-001
		98.43*	12.00	4.88356E+000	9.07786E-001
		111.30*	1.03	7.76854E+000	1.81476E+000
		300.34*	6.62	1.25814E-002	6.85322E-003
		312.17*	38.60	1.12800E-002	2.97103E-003
		340.81	4.47		
U-238+d	0.412	58.54*	1.30	2.69612E+004	5.24199E+003
		63.30	4.80		
		81.91	0.36		
		92.60*	5.60	4.35641E+000	7.85775E-001
		766.36	0.29		
		1001.03	0.84		
Pu-239	1.000	129.30*	0.01	2.84885E+003	3.71903E+002
		203.55*	0.00	2.72220E+003	5.63463E+002
		375.05*	0.00	2.90725E+003	2.92953E+002
		413.71*	0.00	2.78224E+003	2.06138E+002
Am-241	0.999	32.20 @	0.17		

Appendix A.   Example ISOCS Data (continued)

Nuclide Name	Confidence	Energy (keV)		Yield (%)	Activity (nCi/gram)	Activity Uncertainty
Am-241	0.999	43.42	@	0.07		
		55.56	@	0.02		
		59.54*	@	35.90	9.76312E+002	1.92497E+002
		69.76	@	0.00		
		98.97*	@	0.02	2.54795E+003	4.43410E+002
		102.98*		0.02	1.55752E+003	2.61582E+002
		125.30*		0.00	1.20063E+003	1.64940E+002
		662.40*	@	0.00	8.21485E+002	1.77933E+002
Am-241B	0.764	164.69		0.00		
		208.01*		0.00	4.42123E+003	4.61553E+002
		267.58		0.00		
		426.47*	@	0.00	2.40552E+003	1.20328E+003
		619.01*	@	0.00	1.05119E+003	5.89829E+002
		653.02	@	0.00		
		688.72	@	0.00		
AM-243	0.966	74.67*		60.00	1.24105E+000	3.38601E-001
		86.79*		0.31	4.44401E+001	1.64685E+001
		117.60		0.50		
		142.18*		0.11	2.28881E+001	8.52262E+000
CM-243	0.303	67.80	@	0.14		
		99.55*		14.30	4.09809E+000	7.66483E-001
		103.76*		23.00	1.32050E+000	2.39351E-001
		106.13		0.27		
		117.00*		10.80	6.14267E-001	1.04221E-001
		120.97		2.87		
		209.75*		3.29	1.06298E+000	1.27767E-001
		228.18		10.60		
		254.41*	@	0.11	2.39186E+000	1.23894E+000
		272.85	@	0.08		
		277.60		14.00		
		285.46		0.73		
		315.88	@	0.02		
		334.31*	@	0.02	2.89152E+001	4.23381E+000

* = Energy line found in the spectrum.
@ = Energy line not used for Weighted Mean Activity
Energy Tolerance :   1.500 FWHM
Nuclide confidence index threshold =   0.30
Errors quoted at 1.960 sigma

Appendix A.   Example ISOCS Data (continued)

```
C  INTERFERENCE  CORRECTED  REPORT  *****

              Nuclide      Wt mean       Wt mean
  Nuclide       Id         Activity      Activity
  Name       Confidence    (nCi/gram)    Uncertainty

X  CS-137       0.992
   BI-211       0.475    1.493649E-002  3.544674E-003
   NP-236B      0.926    2.847314E-002  4.901607E-003
   NP-237       0.396    1.208661E+000  1.901715E-001
   Np-237B      0.890    1.152688E-002  2.718794E-003
   U-238+d      0.412    4.096278E+000  7.863103E-001
   Pu-239       1.000    2.820630E+003  1.481437E+002
X  Pu-240       0.988
   Am-241   @   0.999    1.116770E+003  1.108810E+002
   Am-241B  @   0.764    1.797112E+003  5.311214E+002
   AM-243       0.966    1.270897E+000  2.353314E-001
   CM-243   @   0.303    6.116242E-001  8.451682E-002

   ? = nuclide is part of an undetermined solution
   X = nuclide rejected by the interference analysis
   @ = nuclide contains energy lines not used in Weighted Mean Activity

C  Errors quoted at  1.960 sigma
```

93

Appendix A.   Example ISOCS Data (continued)

```
..........        ..  .......  .  ......     ....  ...
C
              Peak Locate Performed on:   9/29/2008   12:06:28 PM
              Peak Locate From Channel:   100
              Peak Locate To Channel:     8192

      Peak    Energy      Peak Size in        Peak CPS     Peak      Tol.
      No.     (keV)     Counts per Second   % Uncertainty  Type    Nuclide

        2     49.52       5.4587E+000           8.31
    m 15    170.86        4.1808E-001          23.50        Sum
      19    238.90        2.1807E-001          58.56        Sum
    M 21    297:22        1.0881E-001          38.52
      24    323.09        3.9156E-001          29.00        Sum
    M 25    332.80        1.3719E+000           4.97        Sum
    M 27    345.07        1.1436E+000           5.57
    M 29    368.31        5.1503E-001           8.95        Sum
    m 31    380.40        7.6525E-001           6.36        Sum
      32    392.92        1.1816E+000           7.90
    m 34    422.55        2.1585E-001          14.03        Sum
      36    451.46        3.8471E-001          15.10        Sum
      37    510.99        2.9021E-001          15.42        Sum
      38    583.23        1.3759E-001          27.48        Sum
      39    609.28        1.7451E-001          22.22        Sum
    M 42    722.09        9.5275E-002          20.37        Sum
C   m 43    727.79        2.0015E-002          63.39        Sum
      44    911.33        8.3134E-002          30.44
      45    934.34        2.4757E-002          65.15
      46    968.98        3.5434E-002          59.86
      47   1120.54        4.1377E-002          53.88
      48   1461.30        5.2746E-001           6.93
      49   1765.21        5.6389E-002          22.94
      50   2616.63        1.2464E-001          14.18

     M = First peak in a multiplet region
     m = Other peak in a multiplet region
     F = Fitted singlet

     Errors quoted at  1.960 sigma
C
```

94

Appendix A.   Example ISOCS Data (continued)

```
**********                 N U C L I D E   M D A   R E P O R T                *****
*****************************************************************************

    Detector Name:        6185DIG
    Sample Geometry:
    Sample Title:         SWB NT060209R
    Nuclide Library Used: C:\GENIE2K\CAMFILES\NTS_OSB_TRU_Expanded
```

Nuclide Name	Energy (keV)	Yield (%)	Line MDA (nCi/gram)	Nuclide MDA (nCi/gram)	Activity (nCi/gram)
Na-22	1274.53	99.94	4.7098E-004	4.71E-004	2.4483E-004
CO-60	1173.24	99.90	4.4417E-004	3.56E-004	2.8628E-004
	1332.50	99.98	3.5617E-004		1.9445E-004
CS-137	661.66*	85.21	1.1003E-003	1.10E-003	3.5092E-003
TL-207	897.60	0.24	1.7368E-001	1.74E-001	3.7358E-002
PB-211	74.81	0.22	1.6051E+001	1.13E-002	1.2876E+002
	77.11	0.37	6.0242E+000		-3.3461E+001
	87.30	0.16	7.5263E+000		3.9829E+000
	404.84	3.83	1.5952E-002		-4.6879E-003
	426.99	1.72	3.7717E-002		3.3919E-002
	704.50	0.48	9.6616E-002		1.1091E-002
	766.34	0.71	6.5227E-002		-3.6089E-002
	831.83	3.81	1.1254E-002		-2.6712E-003
	1109.50	0.15	3.0077E-001		1.1922E-001
RA-223	81.07	15.00	1.0264E-001	8.14E-003	1.4023E-002
	83.78	24.80	5.8250E-002		-5.5089E-002
	94.90	11.30	9.8539E-002		5.6420E-001
	122.31	1.19	3.3728E-001		-1.5169E-001
	144.20	3.26	8.0292E-002		9.5738E-002
	154.19	5.59	3.7225E-002		4.3940E-003
	158.62	0.69	2.9927E-001		-1.6412E-002
	179.67	0.15	1.1563E+000		7.4163E-001
	269.41	13.60	8.1409E-003		1.8208E-004
	288.17	0.15	6.6309E-001		4.0328E-001
	323.89	3.90	2.8953E-002		5.5266E-002
	328.50	0.20	4.7220E-001		2.7823E-002
	338.32	2.78	3.8410E-002		-9.6306E-002
	342.90	0.20	6.1482E-001		1.7429E-001
	371.84	0.49	1.9052E-001		-2.4746E+000
	444.94	1.27	4.2309E-002		4.7759E-004
TH-227	50.20	8.50	6.7954E+001	1.13E-002	1.9118E+002
	62.50	0.24	5.8399E+001		-9.9497E+000
	79.77	2.10	7.8333E-001		-1.1378E+000
	85.43	1.61	8.7750E-001		1.8270E+000
	88.47	2.66	4.2931E-001		2.5758E-001
	94.00	1.40	7.9280E-001		3.3667E+000
	100.00	1.22	1.0439E+000		1.1805E+000
	113.20	0.15	3.8698E+000		-2.4567E+001
	113.20	0.56	1.0366E+000		-6.5804E+000
	117.20	0.17	2.7926E+000		4.1229E-001
	141.30	0.13	1.8239E+000		-2.2453E-002
	204.30	0.23	8.9311E-001		5.0517E+000

95

Name	(keV)	(%)	(nCi/gram)	(nCi/gram)	(nCi/gram)
TH-227	205.00	0.15	1.2951E+000	1.13E-002	-4.3553E+000
	206.10	0.23	8.4760E-001		-1.2845E+001
	210.65	1.13	1.3083E-001		1.3371E-002
	234.90	0.45	2.7820E-001		-9.4019E-002
	236.00	11.20	1.1300E-002		4.4570E-004
	250.20	0.37	3.1453E-001		6.6612E-003
	250.40	0.13	8.9531E-001		1.8961E-002
	252.55	0.11	1.0499E+000		-1.1928E-001
	254.70	0.80	1.5786E-001		2.5841E-001
	256.25	6.80	1.8062E-002		1.6106E-002
	273.00	0.49	2.1328E-001		1.5683E-002
	281.40	0.16	6.3930E-001		-4.2209E-001
	286.15	1.60	6.3783E-002		-1.5273E-002
	296.60	0.43	2.6552E-001		3.2195E-001
	299.90	2.00	5.4104E-002		2.2293E-002
	300.30	0.20	5.3145E-001		2.6460E-001
	304.44	1.05	9.2979E-002		-5.6384E-002
	312.66	0.48	2.6424E-001		1.0198E+000
	314.86	0.46	2.1586E-001		9.7743E-002
	329.82	2.80	3.4384E-002		5.7293E-003
	334.40	1.00	1.6597E-001		-1.4931E-001
	342.46	0.35	3.2303E-001		1.8814E-001
	350.50	0.11	8.7483E-001		6.6527E-001
PA-231	255.76	0.10	1.2285E+000	4.45E-002	1.5757E+000
	260.23	0.18	6.1083E-001		-9.3516E-002
	283.67	1.60	6.3664E-002		1.1784E-003
	300.02	2.40	4.4451E-002		2.0411E-002
	302.65	1.60	6.1855E-002		1.4888E-002
	302.65	0.64	1.5464E-001		3.7220E-002
	312.94	0.11	1.0848E+000		2.4694E+000
	330.06	1.30	7.8068E-002		2.7783E-003
	340.80	0.17	6.1677E-001		5.9815E-001
	357.21	0.15	5.6974E-001		1.9277E-001
U-233	42.44	0.06	2.4870E+005	1.10E+001	-8.3054E+004
	54.70	0.01	1.1845E+004		-7.1120E+004
	97.14	0.02	6.2274E+001		-4.0701E+002
	146.35	0.01	4.0762E+001		-7.2920E+001
	164.51	0.01	3.0230E+001		-1.4919E+000
	291.32	0.01	1.9337E+001		2.4302E+000
	317.13	0.01	1.0982E+001		-6.6751E+000
	320.51	0.00	3.4802E+001		-1.6469E+001
U-234	53.20	0.12	1.8928E+003	1.89E+003	-9.9311E+003
U-235	72.70	0.11	3.3364E+001	2.99E-003	3.0651E+001
	89.95	3.55	2.9435E-001		-2.6497E-001
	93.35	5.81	1.7978E-001		-6.3986E-001
	105.00	2.69	2.9904E-001		3.3423E-001
	109.16	1.54	3.8035E-001		-1.4855E+000
	140.76	0.22	1.0786E+000		-1.0487E-001
	143.76	10.96	2.3807E-002		3.6429E-002
	163.33	5.08	4.0657E-002		-1.4730E-002
	182.61	0.34	4.9898E-001		-7.1754E-002

96

Nuclide Name	Energy (keV)	Yield (%)	Nuclide Min (nCi/gram)	Nuclide Ave (nCi/gram)	Activity (nCi/gram)
U-235	185.71	57.20	2.9887E-003	2.99E-003	1.5890E-003
	194.94	0.63	2.6986E-001		4.0402E-001
	202.11	1.08	1.7026E-001		-3.3977E-001
	205.31	5.01	3.7398E-002		-4.3233E-001
+ NP-236B	94.67*	23.40	5.3130E-002	9.45E-003	1.0426E+000
	98.44*	38.00	2.7486E-002		1.5422E+000
	99.55	0.23	6.2481E+000		1.2958E+002
	104.20*	7.20	1.1966E-001		4.2183E+000
	111.00*	17.70	4.0128E-002		4.5207E-001
	158.35	3.96	5.1702E-002		-6.6906E-003
	160.33*	31.50	9.4468E-003		2.6329E-002
+ NP-237	57.10	0.39	3.7141E+002	1.57E-001	-4.4290E+004
	86.48*	12.40	1.5726E-001		1.1110E+000
	87.99	0.14	8.3849E+000		8.0938E+000
	92.29	1.68	5.9886E-001		-3.5996E+000
	94.64*	0.60	2.0721E+000		4.0660E+001
	95.87	2.73	3.8388E-001		-1.7471E+000
	108.00	1.27	4.1593E-001		-1.1266E-001
	117.70	0.16	2.8413E+000		-1.0010E-001
	143.25*	0.43	2.0382E+000		6.0680E+000
	151.41	0.23	9.3927E-001		3.0229E-001
	194.95*	0.18	1.1377E+000		1.3261E+000
	212.29	0.16	8.6593E-001		6.6819E-002
+ Np-237B	29.37	15.00	1.2657E+012	4.52E-003	-3.9692E+012
	86.48*	7.40	2.6351E-001		1.8617E+000
	94.65*	5.62	2.2122E-001		4.3409E+000
	98.43*	12.00	8.7040E-002		4.8836E+000
	111.30*	1.03	6.8958E-001		7.7685E+000
	300.34*	6.62	1.7811E-002		1.2581E-002
	312.17*	38.60	4.5185E-003		1.1280E-002
	340.81	4.47	2.3457E-002		2.2749E-002
Pu-238	152.72	0.00	2.2532E+002	2.25E+002	2.1785E+001
	766.39	0.00	2.1051E+003		-1.1647E+003
	1001.03	0.00	4.3130E+005		8.5538E+004
+ U-238+d	58.54*	1.30	7.9055E+001	5.15E-002	2.6961E+004
	63.30	4.80	1.6689E+000		-8.4937E-001
	81.91	0.36	4.0822E+000		3.5637E-001
	92.60*	5.60	2.2201E-001		4.3564E+000
	766.36	0.29	1.5752E-001		-8.7155E-002
	1001.03	0.84	5.1529E-002		1.0220E-002
+ Pu-239	129.30*	0.01	5.9722E+001	5.71E+001	2.8489E+003
	203.55*	0.00	3.4339E+002		2.7222E+003
	375.05*	0.00	6.7040E+001		2.9073E+003
	413.71*	0.00	5.7059E+001		2.7822E+003
Pu-239B	103.06	0.00	4.6274E+003	1.79E+003	8.0956E+004
	144.35	0.00	1.5304E+004		2.1295E+004
	146.09	0.00	2.1822E+003		-1.3350E+003
	171.39	0.00	1.7896E+003		2.5127E+003
	179.22	0.00	2.6875E+003		2.2768E+003
	189.36	0.00	2.0596E+003		1.4961E+003
Pu-240	160.31*	0.00	7.4023E+002	7.40E+002	2.0631E+003

97

Name	Energy (keV)	Yield (%)	Ldn Act (nCi/gram)	Known Act (nCi/gram)	Activity (nCi/gram)
+ Am-241	32.20	0.17	5.6679E+010	2.86E+000	3.0382E+011
	43.42	0.07	1.1003E+005		-1.5833E+005
	55.56	0.02	7.9364E+003		-3.4192E+004
	59.54*	35.90	2.8627E+000		9.7631E+002
	69.76	0.00	1.3048E+003		9.1332E+001
	98.97*	0.02	4.5412E+001		2.5479E+003
	102.98*	0.02	4.4181E+001		1.5575E+003
	125.30*	0.00	1.0813E+002		1.2006E+003
	662.40*	0.00	2.5757E+002		8.2149E+002
+ Am-241B	164.69	0.00	2.9761E+003	2.31E+002	-1.4688E+002
	208.01*	0.00	2.3144E+002		4.4212E+003
	267.58	0.00	4.4316E+003		6.0490E+003
	426.47*	0.00	3.0512E+003		2.4055E+003
	619.01*	0.00	9.3866E+002		1.0512E+003
	653.02	0.00	1.4745E+003		1.3136E+003
	688.72	0.00	1.5192E+003		4.9841E+002
CM-241	102.05	22.60	4.6859E-002	6.64E-004	-1.0270E-001
	106.49	36.00	1.5899E-002		-4.1213E-003
	120.00	17.10	2.2942E-002		-3.4011E-002
	132.41	3.90	6.9979E-002		-1.3865E-002
	164.80	0.44	4.5276E-001		1.5009E-001
	165.05	2.97	6.7021E-002		2.2217E-002
	180.28	0.48	3.6619E-001		8.6123E-002
	205.88	2.67	7.3020E-002		-1.1065E+000
	265.92	0.40	2.8800E-001		-1.2405E-002
	417.24	0.65	9.3682E-002		-5.3631E-001
	430.63	4.10	1.3414E-002		1.9144E-004
	447.35	0.12	4.4774E-001		1.1639E-001
	463.27	1.23	4.2303E-002		1.8627E-002
	471.80	71.00	6.6420E-004		-1.1661E-004
	504.45	0.59	7.8534E-002		1.7875E-002
	636.88	1.53	2.8483E-002		1.1639E-003
	653.20	0.15	3.7864E-001		3.3732E-001
	670.20	0.57	7.6042E-002		-3.6843E-002
Pu-241	148.57	0.00	1.3566E+003	1.36E+003	2.1603E+003
+ AM-243	74.67*	60.00	1.3329E-001	1.33E-001	1.2411E+000
	86.79*	0.31	6.2903E+000		4.4440E+001
	117.60	0.50	9.1076E-001		-3.2086E-002
	142.18*	0.11	7.6878E+000		2.2888E+001
+ CM-243	67.80	0.14	3.2802E+001	7.74E-003	-2.1312E+001
	99.55*	14.30	7.3041E-002		4.0981E+000
	103.76*	23.00	3.7458E-002		1.3205E+000
	106.13	0.27	2.2533E+000		-5.5452E-001
	117.00*	10.80	6.0033E-002		6.1427E-001
	120.97	2.87	1.3496E-001		-2.1860E-001
	209.75*	3.29	5.5644E-002		1.0630E+000
	228.18	10.60	1.1795E-002		1.9371E-004
	254.41*	0.11	1.8916E+000		2.3919E+000
	272.85	0.08	1.2590E+000		9.2576E-002
	277.60	14.00	7.7357E-003		4.2138E-003
	285.46	0.73	1.4015E-001		-4.9722E-002

98

Appendix A. Example ISOCS Data (continued)

Nuclide Name	Energy (keV)	Yield (%)	Activity (nCi/gram)	MDA (nCi/gram)	Activity (nCi/gram)
+ CM-243	315.88	0.02	5.4035E+000	7.74E-003	5.6678E+000
	334.31*	0.02	5.4326E+000		2.8915E+001
Cm-244	152.62	0.00	2.1557E+002	2.16E+002	-3.9044E+001
	263.33	0.00	1.9783E+003		2.3798E+002
	554.54	0.00	5.5343E+002		-9.9696E+000
	817.87	0.00	5.9778E+002		-4.2720E+002
CM-245	79.25	0.15	1.1421E+001	1.88E-002	-1.2638E+001
	132.99	2.77	9.2661E-002		-3.3803E-002
	136.06	0.11	2.1784E+000		-4.6728E-001
	174.94	9.50	1.8758E-002		3.7200E-003
	189.82	0.19	8.8303E-001		1.0298E+000
CF-249	54.80	0.15	1.0754E+003	1.07E-003	-6.4570E+003
	92.35	0.19	5.1456E+000		-3.0929E+001
	104.61	2.09	4.2388E-001		3.5842E+000
	109.29	3.33	1.7539E-001		-6.8501E-001
	123.00	1.58	2.5724E-001		-9.2541E-002
	241.00	0.19	6.5727E-001		9.3303E-002
	252.87	2.47	4.7056E-002		-4.8770E-004
	266.80	0.40	2.9038E-001		1.1099E-001
	295.80	0.14	8.2391E-001		3.4271E-001
	333.40	14.40	1.2692E-002		5.8462E-002
	388.30	66.00	1.0735E-003		3.8299E-004

+ = Nuclide identified during the nuclide identification
* = Energy line found in the spectrum
> = MDA value not calculated
@ = Half-life too short to be able to perform the decay correction

99

Appendix B.   Standard Waste Box Data Sheet

|	
Program Coordinator: Gerald Woolsey	
Date: 08/10/06	

Name of product	Procurement Lead Time	Catalog Number
Standard Waste Box (SWB)	10 weeks	

Reference Documents

a) *WP 08-PT.01, Standard Waste Box Handling and Operation Manual Rev 5*

b) E-I-343, Specification for Fabrication of the Standard Waste Box, Rev 9

c) Quality Assurance Inspection Plan for the Standard Waste Box Inventory WP 13-QA.19, Rev. 2

d) 165-F-001-W Series, Standard Waste Box Assembly, Rev V

1.0   General Description
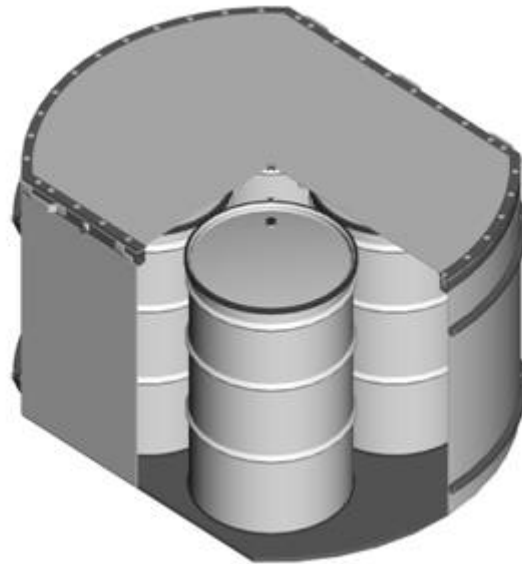
Standard Waste Box

Appendix B.   Standard Waste Box Data Sheet (continued)

Table 1 – SWB Weights

Component	Weight (pounds)		
	Maximum Gross	**Nominal Tare**	**Net Content**
SWB	4,000	640	3360

Table 2 – SWB Dimensions

Dimension	Approximate Measurement (Inches)	
	Inside	**Outside**
Height	36 9/16	36 7/8
Length	68 ¾	71
Width	52	54 ½

2.0   Container Performance Criteria

The SWB was qualified by the U.S. Department of Energy (USDOE) in 1988 as meeting the U.S. Department of Transportation (USDOT) requirements for Specification 7A Type A packagings. Qualification has been documented in the USDOE, *DOE/RL-96-57 (Volumes 1 and 2), Test and Evaluation Document for the U.S. Department of Transportation Specification 7A TYPE A Packaging*, under Docket Number 89-07-7A and 98-45-7A.

U.S. DOT 7A Compliance Documents -

49 CFR §173.465, Type A Packaging Tests

3.0   Quality Assurance

The Seller's C of C shall be signed by an officer of the Sellers' Organization, certifying the conformance of the supplied items to the requirements of this specification (including contract drawings). The Certificate of Compliance/Conformance (C of C) shall be traceable to the serial number(s) of the component(s).

4.0   Suggested Manufacturers –specified in the BOA

101

Appendix C. Example SuperHENC Data

Version Information
NGI Version: 2.00
SUPRHENC Analysis SW Version: 1.03   PCFRAM Analysis Version: 4.4
Calculation DLL: 2.00, License File DLL: 1.00, Password DLL: 1.10, Report DLL: 1.10
Neutron Data Import DLL: 1.00, Gamma Data Import DLL: 1.10, Data Archive DLL: 1.00
NT060209R.akl Version: 3.2, NGI.GLB Version: 3.00, NGI.MDA Version: 3.0, NGI.TMU Version: 3.0

Identifying Data
Radioassay Procedure: CCP-TP-146 Rev6
Facility: INL
Neutron Assay Date and Time: 04\03\2009 09:58:59   Gamma Assay Date and Time: 04\03\2009 09:25:50
SUPRHENC Filename 943J5859.ASA   PCFRAM Filename: nt060209r.res
NGI results File: C:\NGIFiles\NGI\NGI_Results\nt060209r.ngi

Tare Weight: 290.90 kg   Gross Weight: 614.90 kg   Net Weight: 324.00 kg
IDC: 99   Is RCRA: No   Imported Material Type: SWB Crate
Gamma Live Time: 890.00 s   Gamma Real Time: 900.00 s   Gamma Percent Dead Time: 1.11
Neutron Cont. ID: NT060209R   Gamma Cont. ID: Unknown
Neutron Equipment ID: Super HENC Gamma Equipment ID: Unknown
Neutron User ID: Rick Green   NGI Analyst ID: S_A_MCELHANEY
Imported Pu240e Mass: 1.183000 g Imported Pu240e Mass Uncertainty: 0.041000 g
Corrected Pu240e Mass: 1.183000 g Corrected Pu240e Mass TMU: 0.051285 g

AAS Correction Factor: 0.998000
PCFRAM Parameter Set: Coax_DWAS_250_rev1 (2006.07.18 03:52)0   Coax 0.25 kev/ch0results file:

Isotope	Fraction (g/gPu)	Fraction Uncertainty (g/gPu)	Mass (g)	Mass TMU at 1-Sigma (g)	Activity (Ci)	Activity TMU at 1-Sigma (Ci)	Rule Used
Pu238	1.0500e-004	4.1000e-005	2.1348e-003	8.5340e-004	3.6931e-002	1.4764e-002	AK Forced
Pu239	9.4060e-001	4.9000e-003	1.9123e+001	1.7893e+000	1.2029e+000	1.1255e-001	AK Forced
Pu240	5.7200e-002	4.8000e-003	1.1629e+000	5.1022e-002	2.6747e-001	1.1735e-002	AK Forced
Pu241	1.7300e-003	3.2003e-004	3.5173e-002	7.2887e-003	3.6580e+000	7.5802e-001	AK Forced
Pu242	4.3000e-004	2.2000e-004	8.7423e-003	4.4918e-003	3.4707e-005	1.7833e-005	AK Forced
Am241	5.7265e-003	2.6628e-004	1.1643e-001	1.2156e-002	4.0400e-001	4.2159e-002	PRAM
Np237	3.4780e-004	3.3284e-005	7.0711e-003	9.4569e-004	5.0417e-006	6.7428e-007	PRAM
U235	< LLD						< LLD
Am243	< LLD						< LLD
Cs137	< LLD						< LLD
U233	< LLD						< LLD
U238	< LLD						< LLD
Cm244	< LLD						< LLD
Ra226	0.0000e+000	0.0000e+000	0.0000e+000	0.0000e+000	0.0000e+000	0.0000e+000	Not In AK
U234	< LLD						< LLD
Sr90	< LLD						< LLD

AK Set Selected: 85400-WG

	Value	TMU at 1-Sigma
Total Thermal Power (Watts):	6.0463e-002	5.7495e-003
Total Plutonium Mass (g):	2.0331e+001	1.8994e+000
Total Pu239 FGE (g Pu239 FGE):	1.9231e+001	1.7995e+000
Total Pu239 Equivalent Activity (PE-Ci):	1.9797e+000	1.8828e-001
Total Alpha Activity (Ci):	1.9114e+000	1.8163e-001
Total TRU Alpha Activity (Ci):	1.9113e+000	1.8163e-001
Total TRU Alpha Activity Concentration (nCi/g):	5.8991e+003	5.6057e+002

MDA (g-Pu240e): 0.018667
MDC (nCi/g): 73.090959
FGE For Criticality Control: 22.758193 (g Pu239 FGE)

Warning Messages
Gamma File Container ID: Unknown differs from Neutron File Container ID:NT060209R
Gamma File Equipment ID: Unknown differs from Neutron File Equipment ID:Super HENC
AKL Filename has been Overridden.
Material Type has been Overridden.
Assay Identification Parameters (SuperHENC User ID and/or Radio-Assay Procedure) have been Overridden.
No KAPPA field found for the "SWB Crate" waste stream. Default first AKL KAPPA value of 1270000000.000000 will be used.
Isotope Pu239 Equivalent Activity Calculation had denominator of 0.00.

Operator Name: Rick Green   Operator Signature: Date: 4/20/09

Reviewer Name: Shae Barber   Reviewer Signature: Date: 4/20/2009

14

Appendix D. Pu-239 Assay Data for SuperHENC and ISOCS

Container	SuperHENC		ISOCS	
	Ci	Uncertainty (Ci) 1-σ	Ci	Uncertainty (Ci) 1-σ
NT070692R	1.97×10^0	1.90×10^{-1}	1.42×10^0	3.82×10^{-2}
NT070688R	1.8902×10^0	1.82×10^{-1}	1.36×10^0	3.87×10^{-2}
NT070724R	1.63×10^0	1.58×10^{-1}	9.34×10^{-1}	2.51×10^{-2}
NT070707R	1.61×10^0	1.60×10^{-1}	1.42×10^0	4.05×10^{-2}
NT070695R	1.51×10^0	1.38×10^{-1}	9.77×10^{-1}	2.74×10^{-2}
NT070683R	1.3462×10^0	1.47×10^{-1}	1.22×10^0	2.80×10^{-2}
NT070691R	1.34×10^0	1.95×10^{-1}	1.11×10^0	3.01×10^{-2}
NT070702R	1.26×10^0	1.18×10^{-1}	1.16×10^0	3.79×10^{-2}
NT060209R	1.2029×10^0	1.13×10^{-1}	9.09×10^{-1}	2.43×10^{-2}
NT080337R	1.11×10^0	1.67×10^{-1}	2.42×10^{-1}	7.83×10^{-3}
NT080263R	9.33×10^{-1}	8.77×10^{-2}	6.55×10^{-1}	2.01×10^{-2}
NT080266R	8.70×10^{-1}	8.84×10^{-2}	4.61×10^{-1}	1.30×10^{-2}
NT080262R	8.45×10^{-1}	8.99×10^{-2}	4.43×10^{-1}	1.69×10^{-2}
NT080328R	8.06×10^{-1}	8.10×10^{-2}	3.46×10^{-1}	1.11×10^{-2}
NT070677R	7.75×10^{-1}	1.28×10^{-1}	8.99×10^{-1}	2.45×10^{-2}
NT070709R	7.66×10^{-1}	2.13×10^{-1}	4.79×10^{-1}	1.44×10^{-2}
NT070705R	7.11×10^{-1}	9.66×10^{-2}	1.04×10^0	2.91×10^0
NT080346R	6.62×10^{-1}	6.01×10^{-2}	4.94×10^{-3}	2.52×10^{-3}
NT080348R	6.48×10^{-1}	9.66×10^{-2}	4.12×10^{-2}	2.10×10^{-2}
NT080259R	6.32×10^{-1}	1.00×10^{-1}	1.14×10^0	3.62×10^{-2}

Appendix D. Pu-239 Assay Data for SuperHENC and ISOCS (continued)

Container	SuperHENC		ISOCS	
	Ci	Uncertainty (Ci) 1-σ	Ci	Uncertainty (Ci) 1-σ
NT080336R	5.92×10^{-1}	6.43×10^{-2}	5.16×10^{-1}	1.52×10^{-2}
NT070720RA	5.85×10^{-1}	1.06×10^{-1}	7.24×10^{-1}	1.79×10^{-2}
NT080255R	5.30×10^{-1}	1.43×10^{0}	3.92×10^{-1}	1.01×10^{-2}
NT070686R	5.06×10^{-1}	6.80×10^{-2}	6.56×10^{-1}	1.63×10^{-2}
NT070703R	4.43×10^{-1}	6.45×10^{-2}	8.08×10^{-1}	2.03×10^{-2}
NT070722R	4.40×10^{-1}	3.84×10^{-2}	3.94×10^{-1}	1.37×10^{-2}
NT070681R	4.17×10^{-1}	3.88×10^{-2}	5.48×10^{-1}	1.81×10^{-2}
NT070679R	3.97×10^{-1}	1.42×10^{-1}	4.02×10^{-1}	1.31×10^{-2}
NT070685R	3.96×10^{-1}	7.85×10^{-2}	4.41×10^{-1}	1.29×10^{-2}
NT070678R	3.91×10^{-1}	5.32×10^{-1}	6.18×10^{-1}	1.55×10^{-2}
NT080341R	3.88×10^{-1}	4.69×10^{-2}	2.45×10^{-1}	7.66×10^{-3}
NT070728R	3.77×10^{-1}	4.28×10^{-2}	3.02×10^{-1}	1.04×10^{-2}
NT080333R	3.71×10^{-1}	4.30×10^{-2}	2.16×10^{-1}	7.21×10^{-3}
NT070689R	3.63×10^{-1}	3.65×10^{-2}	3.42×10^{-1}	9.77×10^{-3}
NT070711R	3.59×10^{-1}	4.97×10^{-2}	3.05×10^{-1}	1.04×10^{-2}
NT080257R	3.36×10^{-1}	4.30×10^{-2}	2.72×10^{0}	6.68×10^{-2}
NT070718R	3.27×10^{-1}	3.23×10^{-2}	1.31×10^{-1}	5.93×10^{-3}
NT070687R	3.18×10^{-1}	3.16×10^{-2}	2.96×10^{-1}	9.41×10^{-3}
NT070719R	2.89×10^{-1}	4.27×10^{-2}	2.96×10^{-1}	8.68×10^{-3}
NT070684R	2.83×10^{-1}	3.19×10^{-2}	2.92×10^{-1}	1.08×10^{-2}

Appendix D. Pu-239 Assay Data for SuperHENC and ISOCS (continued)

Container	SuperHENC		ISOCS	
	Ci	Uncertainty (Ci) 1-σ	Ci	Uncertainty (Ci) 1-σ
NT070704R	2.58×10^{-1}	3.10×10^{-2}	1.08×10^{-1}	3.78×10^{-3}
NT070723R	2.42×10^{-1}	2.66×10^{-2}	2.39×10^{-1}	7.96×10^{-3}
NT080258R	2.40×10^{-1}	2.47×10^{-2}	2.17×10^{-1}	6.08×10^{-3}
NT080349R	1.98×10^{-1}	1.91×10^{-2}	7.91×10^{-2}	7.98×10^{-3}
NT060211RA	1.89×10^{-1}	6.37×10^{-2}	4.64×10^{-2}	2.26×10^{-3}
NT070690R	1.67×10^{-1}	3.29×10^{-2}	1.85×10^{-1}	7.46×10^{-3}
NT070721R	1.58×10^{-1}	2.45×10^{-2}	8.90×10^{-2}	4.49×10^{-3}
NT070694R	1.52×10^{-1}	2.23×10^{-2}	7.99×10^{-1}	2.05×10^{-2}
NT070706R	1.43×10^{-1}	2.56×10^{-2}	6.35×10^{-2}	4.20×10^{-3}
NT080261R	1.34×10^{-1}	2.41×10^{-2}	3.24×10^{-1}	9.46×10^{-3}
NT080330R	1.33×10^{-1}	1.95×10^{-2}	2.84×10^{-1}	8.58×10^{-3}
NT070693R	1.26×10^{-1}	2.10×10^{-2}	3.55×10^{-1}	1.11×10^{-2}
NT070729R	1.19×10^{-1}	1.88×10^{-2}	3.07×10^{-1}	8.85×10^{-3}
NT070680R	1.08×10^{-1}	1.88×10^{-2}	3.36×10^{-2}	2.15×10^{-3}
NT070712R	1.07×10^{-1}	1.79×10^{-2}	1.78×10^{-1}	8.68×10^{-3}
NT080256R	8.99×10^{-2}	1.42×10^{-2}	2.90×10^{-1}	9.55×10^{-3}
NT080342R	8.54×10^{-2}	4.74×10^{-2}	2.34×10^{-1}	9.08×10^{-3}
NT080340R	8.36×10^{-2}	1.38×10^{0}	1.16×10^{-1}	6.49×10^{-3}
NT070676R	8.34×10^{-2}	1.51×10^{-2}	1.53×10^{-2}	1.95×10^{-3}
NT080335R	8.34×10^{-2}	2.55×10^{-2}	6.47×10^{-2}	2.69×10^{-3}

105

Appendix D. Pu-239 Assay Data for SuperHENC and ISOCS (continued)

Container	SuperHENC		ISOCS	
	Ci	Uncertainty (Ci) 1-σ	Ci	Uncertainty (Ci) 1-σ
NT080339R	7.32×10^{-2}	1.56×10^{-2}	1.34×10^{-1}	5.49×10^{-3}
NT080329R	7.07×10^{-2}	6.95×10^{-2}	3.51×10^{-1}	1.63×10^{-2}
NT060208R	6.92×10^{-2}	1.11×10^{-2}	2.22×10^{-1}	9.46×10^{-3}
NT080331R	5.90×10^{-2}	3.19×10^{-2}	4.40×10^{-1}	3.39×10^{-2}
NT060212R	5.49×10^{-2}	2.69×10^{-2}	6.15×10^{-2}	5.71×10^{-3}
NT070699R	5.49×10^{-2}	2.39×10^{-2}	5.17×10^{-2}	3.10×10^{-3}
NT080338R	4.97×10^{-2}	7.61×10^{-3}	1.43×10^{-1}	7.30×10^{-2}
NT070715RA	3.42×10^{-2}	4.63E-003	1.06×10^{-1}	6.42×10^{-3}
NT080344R	2.73×10^{-2}	1.31E-002	9.15×10^{-2}	4.67×10^{-2}
NT070701R	2.57×10^{-2}	1.02E-002	8.89×10^{-2}	4.29×10^{-3}
NT070682R	2.24×10^{-2}	6.25E-003	1.06×10^{-1}	4.53×10^{-3}
NT070713R	1.95×10^{-2}	1.06E-002	3.98×10^{-2}	3.82×10^{-3}
NT060207R	9.92×10^{-3}	1.60E-003	8.91×10^{-2}	4.60×10^{-3}
NT070714R	8.80×10^{-3}	1.64E-003	1.88×10^{-1}	6.73×10^{-3}
NT080260R	6.58×10^{-3}	2.47E-003	1.48×10^{-1}	6.20×10^{-3}
NT060210R	3.74×10^{-3}	2.57E-003	9.45×10^{-2}	4.02×10^{-3}
NT080334R	3.31×10^{-3}	1.72E-003	4.11×10^{-2}	4.88×10^{-3}

Appendix E.   Example Raw ISOCS Detector Data

	Energy (keV)	FWHM (keV)	Net Peak Area	Net Area Uncertainty	Continuum Counts
NT060207R					
129.3	129.3	1.57	1.85×10^3	479.64	9.62×10^3
375.05	374.8	1.72	5.79×10^2	61.11	3.82×10^2
413.71	413.42	1.65	5.42×10^2	81.34	2.39×10^2
NT060208R					
129.3	129.4	1.73	4.83×10^3	837.96	3.54×10^4
203.55	204.23	1.94	7.29×10^2	506.98	1.55×10^4
375.05	375.16	1.81	1.19×10^3	98.18	1.74×10^3
413.71	413.88	1.96	1.02×10^3	143.66	8.69×10^2
NT060209R					
129.3	129.35	1.72	2.22×10^4	346.94	9.86×10^3
203.55	203.62	1.71	2.56×10^3	149.66	4.74×10^3
375.05	375.11	1.93	6.57×10^3	171.08	1.02×10^3
413.71	413.75	1.76	5.71×10^3	156.33	6.05×10^2
NT060210R					
129.3	129.4	1.55	2.89×10^3	209.52	9.43×10^3
203.55	203.71	1.24	2.15×10^2	95.62	2.91×10^3
375.05	374.98	1.74	6.19×10^2	65.9	5.38×10^2
413.71	413.69	1.35	5.98×10^2	92.18	3.41×10^2

107

Appendix E. Example Raw ISOCS Detector Data (continued)

	Energy (keV)	FWHM (keV)	Net Peak Area	Net Area Uncertainty	Continuum Counts
NT060211R					
129.3	129.51	1.59	6.62×10^3	206.43	4.86×10^3
203.55	203.8	1.51	9.36×10^2	101.32	2.48×10^3
375.05	375.54	1.67	2.51×10^3	109.16	5.84×10^2
413.71	414.22	1.78	2.42×10^3	140.07	4.69×10^2
NT060211RA					
129.3	129.23	0.98	2.67×10^3	439.51	5.20×10^3
203.55	203.54	1.01	2.46×10^2	64.04	1.20×10^3
375.05	375.05	1.3	5.30×10^2	57.23	3.12×10^2
413.71	413.68	1.74	5.93×10^2	97.18	3.12×10^2
NT070676R					
129.3	129.16	1.5	7.83×10^2	296.72	3.67×10^3
375.05	375.05	1.63	1.60×10^2	85.99	3.52×10^2
413.71	413.4	1.44	1.93×10^2	73.93	2.45×10^2
NT070677R					
129.3	129.34	1.46	1.78×10^4	322.33	9.88×10^3
203.55	203.55	1.49	2.79×10^3	159.84	5.13×10^3
375.05	375.04	1.7	7.55×10^3	187.75	1.12×10^3
413.71	413.68	1.7	7.12×10^3	213.66	8.81×10^2

Appendix F.   Example MCNP Input File

Modeling of Standard Waste Boxes - J. Miller Master's Thesis

c **************** Block 1: Cell Cards ******************

c   Waste mixture inside SWB

 1   1   -0.01   20 -30 60 -70 100 -110 IMP:P=1

c   No SWB

 2   3   -0.001275   10 -40 50 -80 90 -120 (-20:30:-60:70:-100:110) IMP:P=1

c   Atmosphere

 3   3   -0.001275 10 -210 230 -90 250 -260 IMP:P=1

 6   3   -0.001275 10 -210 120 -240 250 -260 IMP:P=1

 7   3   -0.001275 10 -210 90 -120 250 -50 IMP:P=1

 8   3   -0.001275 10 -210 90 -120 -260 80 IMP:P=1

 9   3   -0.001275 40 -210 50 -80 90 -120 IMP:P=1

c   Ground (Dry Sand with Gravel)

 4   4   -1.650   -10 220 230 -240 250 -260 IMP:P=1

c   void around the problem

109

www.manaraa.com

 5 0   210:-220:-230:240:-250:260   IMP:P=0

c **************** Block 2: Surface Cards ***************

c SWB modeled as a rectangular cube with wall thickness of 0.4 cm,

 10 PZ   0.0 $ Bottom Outside of SWB

 20 PZ   0.4 $ Bottom Inside of SWB

 30 PZ   93.3 $ Top Inside of SWB

 40 PZ   93.7 $ Top Outside of SWB

 50 PY   0.0 $ Front Outside of SWB

 60 PY   0.4 $ Front Inside of SWB

 70 PY   132.5 $ Back Inside of SWB

 80 PY   132.9 $ Back Outside of SWB

 90 PX   0.0 $ Left Outside of SWB   (approximate shape)

 100 PX   0.4 $ Left Inside of SWB   (approximate shape)

 110 PX   175.0 $ Right Inside of SWB   (approximate shape)

```
120 PX   175.4              $ Right Outside of SWB  (approximate shape)

c  130 RCC   224.94 296.87 47 1.51 1.99 0 2  $ Detector at 1/2 z, 60 in. away

210 PZ   200.0              $ Top of world

220 PZ   -50.0              $ Bottom of world

230 PX   -50.0              $ Left of world

240 PX   500.0              $ Right of world

250 PY   -50.0              $ Front of world

260 PY   500.0              $ Back of world


c ***************** Block 3: Data Cards *******************

M1   26000  -0.9799         $ Waste Iron mass fraction (approximate)

     6000  -0.02            $ Waste Carbon mass fraction (approximate)

     94239  -0.0001         $ Waste Plutonium mass fraction (approximate)

M2   26000  -0.98           $ SWB Iron mass fraction (approximate)

     6000  -0.02            $ SWB Carbon mass fraction (approximate)
```

Appendix F.   Example MCNP Input File (continued)

M3   7000 78 $ Atmospheric Nitrogen

     8000 21 $ Atmospheric Oxygen

      18000   1 $ Atmospheric Argon

M4   14000   1 $ Sand - Silicon

     8000   2 $ Sand - Oxygen

MODE P $ Photon Transport only (Table 4-1)

PHYS:P $ Photons - 5.4.2.2

c Source Definition 5.5.1

SDEF CEL=1 ERG=d1 X=d2 Y=d3 Z=d4 PAR=2 $ Photons in Cell 1

c SI-Source Information 5.5.1.1 SP-Source Probability 5.5.1.2

SI1 L 0.1293 0.20355 0.37505 0.41371 $ Discrete energies for Pu-239

SP1 0.00631 0.000569 0.00155 0.00147 $ Probabilities per BNL

SI2 0.4 150   175.0 $ X bounds of waste

SP2 0   0.05 0.95 $ Bias away from detector (X axis)

SI3 0.4 132.5 $ Y bounds of waste

Appendix F.   Example MCNP Input File (continued)

SP3 0 1 $ Equal probability on Y axis

SI4 0.4 93.3 $ Z bounds of waste

SP4 0 1 $ Equal probability on Z axis

c Tallies

F1:P 120 $ Surface Tally 5.6.1 and 5.6.1.1

c Tally Energy 5.6.3

E1 0.128 0.129 0.130 0.131 0.203 0.204 0.375 0.376 0.413 0.414 0.5

c other

PRINT 50 110 128 130 161 162 $ Output Print Tables 5.8.4

NPS 100000000 $ History Cutoff 5.8.1